



Original Article

CFD approach to modelling, hydrodynamic analysis and motion characteristics of a laboratory underwater glider with experimental results

Yogang Singh*, S.K. Bhattacharyya, V.G. Idichandy

Department of Ocean Engineering, Indian Institute of Technology-Madras, Chennai, India

Received 17 November 2016; received in revised form 3 February 2017; accepted 26 March 2017

Available online 9 April 2017

Abstract

Underwater gliders are buoyancy propelled vehicle which make use of buoyancy for vertical movement and wings to propel the glider in forward direction. Autonomous underwater gliders are a patented technology and are manufactured and marketed by corporations. In this study, we validate the experimental lift and drag characteristics of a glider from the literature using Computational fluid dynamics (CFD) approach. This approach is then used for the assessment of the steady state characteristics of a laboratory glider designed at Indian Institute of Technology (IIT) Madras. Flow behaviour and lift and drag force distribution at different angles of attack are studied for Reynolds numbers varying from 10^5 to 10^6 for NACA0012 wing configurations. The state variables of the glider are the velocity, gliding angle and angle of attack which are simulated by making use of the hydrodynamic drag and lift coefficients obtained from CFD. The effect of the variable buoyancy is examined in terms of the gliding angle, velocity and angle of attack. Laboratory model of glider is developed from the final design asserted by CFD. This model is used for determination of static and dynamic properties of an underwater glider which were validated against an equivalent CAD model and simulation results obtained from equations of motion of glider in vertical plane respectively. In the literature, only empirical approach has been adopted to estimate the hydrodynamic coefficients of the AUG that are required for its trajectory simulation. In this work, a CFD approach has been proposed to estimate the hydrodynamic coefficients and validated with experimental data. A two-mass variable buoyancy engine has been designed and implemented. The equations of motion for this two-mass engine have been obtained by modifying the single mass version of the equations described in the literature. The objectives of the present study are to understand the glider dynamics adopting a CFD approach, fabricate the glider and its variable buoyancy engine and test its trajectory in water and compare it with numerically obtained trajectory in the vertical plane.

© 2017 Shanghai Jiaotong University. Published by Elsevier B.V.

This is an open access article under the CC BY-NC-ND license. (<http://creativecommons.org/licenses/by-nc-nd/4.0/>)

Keywords: AUG; CFD; Drag; Glider; Underwater glider; Variable buoyancy engine.

1. Introduction

In the past, the ocean interior was mainly observed using instruments lowered from research ships or suspended from moorings. Typical ship cruises last about a month or two while moorings may last a year or two. The relatively high cost of these observation platforms has limited their number and consequently, the ocean data gathering capability had been limited. The advent of satellite navigation and communication made a class of small, inexpensive instrument platforms possible that are changing the way the ocean is

observed. Autonomous underwater vehicle (AUV), Remotely operated vehicle (ROV) and Autonomous underwater glider (AUG) are the main underwater platforms available today that play an important role in marine environmental data acquisition applications.

An underwater glider changes its buoyancy to go down from or come up to the free surface covering the required depth of observation. The horizontal or forward motion is generated by the lift force generated by its wings. This forward component of lift force will be present during both ascent and descent, so the trajectory followed by an AUG resembles a sawtooth profile. The observation system consisting of sensors will be active during the gliding motion that collects the required data and when the glider ascends to the

* Corresponding author.

E-mail address: yogang.singh@plymouth.ac.uk (Y. Singh).

surface of the ocean, the acquired data will be transmitted to control centres or research vessels using satellite or other communication system. The forward motion of the glider can be used to counter the head-on currents. Glider motion is governed by buoyancy control, pitch control and heading control. Buoyancy control is achieved by controlling the mass flow rate of the pump in injecting and ejecting fluid through a bladder or the frequency of the single stroke piston pumps in extending and retracting a piston in a cylinder. This control is mainly responsible for the major pitching effect in piston based gliders while in bladder based gliders such as Spray and Seaglider, this causes relative change in the positions of the centre of buoyancy and the centre of gravity creating a moment that pitches the glider. Pitch control can be typically controlled by shifting an internal mass fore and aft within the glider. Fine control of pitching angle can be achieved by this shifting. Two methods for controlling heading are currently used. The most intuitive method is by deflecting a rudder to induce a yaw moment. The other method is to rotate an eccentric mass about a longitudinal axis of glider causing the glider to roll and thus allowing a component of the lift force to act laterally, producing a spiral motion. Gliders that roll to turn achieve a turning radius of 20–30 m and are more suited for deep sea operations while rudder based heading control is more suited for shallow water operation and induce a tighter turning circle of about 7 m [3].

The AUGs can travel thousands of kilometres before they are retrieved. They can be operated in a wide range of depths where shipboard measurements are difficult to carry out. Major applications of gliders include scientific [17], and defence / naval applications [19]. Gliders make measurements of oceanographic parameters such as temperature, conductivity (which is used to compute salinity), current speed and direction, depth, optical backscatter, acoustic backscatter, chlorophyll fluorescence, etc. They are, therefore, very useful in areas such as bathymetric survey, ocean acoustics, ocean optics and ocean pollution monitoring. In naval applications, gliders are used in the tasks associated with maritime intelligence, surveillance and reconnaissance (ISR), mine detection, anti-submarine warfare (ASW), real time command, control, and communications (C3) and harbour patrolling.

1.1. Review of literature

Stommel [23] first introduced the concept of an underwater glider. There are currently three types of gliders, namely, electric gliders that change buoyancy using a battery powered pump; thermal gliders that harness energy from the ocean's temperature gradient and hybrid gliders that use battery powered propellers for propulsion together with battery powered pump for changing buoyancy. Webb et al. [27] discussed the design details and field trial results of Slocum electric as well as Slocum thermal gliders, highlighting their limitations and operational capabilities. Eriksen et al. [5] reported development and operation of Seaglider and results of its field trials. Sherman et al. [22] discussed the development of Spray glider and reported the results of the field test. Davis et al. [3]

reported a comparative analysis of commercial gliders and their design characteristics. Rudnick et al. [20] discussed glider designs of Slocum, Spray and Seaglider and their capabilities to contribute towards ocean research infrastructure. Underwater gliders such as Slocum [27], Seaglider [5], Spray [22], Slocum thermal [27], X-Ray [19] and Deep glider [19] have already been tested in oceanographic research and littoral survey missions. Slocum, Spray and Seaglider are termed 'legacy gliders' [25].

Gliders move with a slow speed and consequently have a low drag that permits long-duration operation. Higher lift to drag ratio is a desirable property for maximum range and higher mission durations of a glider. Gliders operating in deep sea environment such as Seaglider have a low drag hull with a high lift to drag ratio. Proper choice of wing hull configuration is required to ensure optimized energy consumption and drag. Model experiments and numerical evaluation using CFD are conducted on glider to study its drag, lift to drag ratio and stability. Geisbert et al. [7] determined hydrodynamic parameters for Slocum, X-Ray and Virginia Tech miniature AUV using computational flight test and semi-empirical approach. Seo et al. [21] developed a simulation program for pitch control using CFD analysis to help develop AUG rationally. Ichihashi et al. [12] used CFD to estimate hydrodynamic forces for various angles of attack and flow speeds for the development of 'Alex' glider that has independently controllable main wing. Du et al. [4] also used CFD in the hydrodynamic design of a glider. Jianguo et al. [14] performed CFD analysis of a hybrid glider 'Petrel' and discussed the effect of wings, rudder and propeller on drag, lift to drag ratio and stability. Ting et al. [25] investigated hydrodynamic characteristics of a glider using CFD analysis. Zhang et al. [30] performed CFD analysis as a stage of the design process of AUG to design a miniature glider. Zhang et al. [31] applied CFD technique to compute hydrodynamic coefficients for 'Seawing' glider to simulate its spiralling motion.

Variable buoyancy (VB) capability enables gliders to enhance functionality and save energy. Larger change in buoyancy achieves higher gliding velocity at desired gliding angles resulting in higher endurance. It is imperative to select variable buoyancy systems providing larger buoyancy changes with lower power requirement. Bladder based systems are more efficient and consume less power in deep sea operation while single-stroke pump based systems are more efficient and consume less power in shallow water operations [10]. Bagley et al. [2] filed a patent and proposed a buoyancy control system for unmanned underwater vehicles. Worall et al. [28] developed a VB engine for deepwater vehicles. Tangirala et al. [24] developed a VB engine and its control software to operate AUV 'Seahorse' in depth and pitch control mode. Zhao et al. [32] developed a bladder based VB engine driven by hydraulic pump for long range AUV. Wang et al. [26] provided theoretical and finite element based formulations to design VB engines in accordance with the operational depth of AUVs.

Modelling the dynamics of a glider is necessary to predict its performance, developing improved control and

navigation algorithms and its design. Over the years, studies have been conducted to improve the motion performance of gliders through better control techniques and navigation algorithms, making use of its dynamic model. Graver et al. [9] discussed the parametric identification of an underwater glider model. Graver et al. [10] discussed the design and preliminary analysis of a small underwater vehicle designed to test and demonstrate the dynamics of gliding. Leonard and Graver [15] proposed equations of motion of glider in the vertical plane by making use of a model based feedback control algorithm. Graver [8] modelled the dynamics of a glider and applied it towards the analysis of glider control, navigation and design. Mahmoudian [18] presented the numerical implementation of a feedback / feed forward control algorithm for improved motion performance of gliders. Fan et al. [6] developed a prototype glider based on a dynamic model of glider and validated it by experimental results.

1.2. Major contributions

To the best of the author's knowledge, no effort is found in the literature that uses the hydrodynamic coefficients obtained from CFD in the simulation of the equations with experimental validation of the glider trajectory. Moreover, a particular glider is a patented technology for which the principal characteristics are explained qualitatively in literature. Their quantitative characteristics and behaviour are not available in the open literature, probably because of legal and copyright issues since these are owned by corporations involved with production and marketing of gliders. Graver [8] suggested modification of equations of motion for multiple moving masses. However, no experimental validation of equations of motion for multiple moving masses exists in the literature. This paper makes an effort in these two directions of involving CFD to evaluate the glider performance as well as experimental validation towards understanding glider dynamics using multiple moving masses. The main objective of the present work is to design and develop a laboratory scale glider and to carry out experimental gliding tests with it in order to establish its dynamics by comparing the experimental gliding trajectory with that obtained from the solution of its equations of motion in the vertical plane using hydrodynamic coefficients obtained from CFD approach.

The present model of the underwater glider is built with a motive to develop a laboratory based platform which can be used to test effectiveness of various guidance, navigation and control approaches within the laboratory which can act as foundation towards development of full scaled model for sea trials. At present in India, no such platform exist which can act as groundwork towards setting guidelines for design and development of full scale models for sea trials.

This section presents the introduction, literature review and the main objective of the present work. Section 2 deals with the analytical formulation of their steady state motion of glider followed by its equations of motion in the vertical plane following the literature. Section 3 presents the CFD approach to the calculation of drag and lift forces that act on

a glider and its validation with the results of a glider available in the literature. Section 4 presents the application of the CFD approach to the laboratory glider to determine its hydrodynamic coefficients considering two wing profiles and presents the steady state motion of the glider. Section 5 deals with design and development of the laboratory glider as part of this work. Section 6 describes the experimental results of the glider trajectory and their verification with the simulation results based on the equations of motion. The final section deals with conclusions of the study.

2. Mathematical model of glider motion in vertical plane

2.1. Kinematic and dynamic model for steady state analysis

Leonard and Graver [15] derived the equation of motions of glider in the vertical plane and described the mathematical model of the steady state dynamics of glider in the longitudinal plane. The steady state gliding motion of glider is defined as: "for a particular change in buoyancy and fixed position of moving mass, the state variables of the glider remain unchanged and angular velocity remains zero for its sawtooth gliding motion" (Zhang et al., 2012). The equation of motions caters to the transient state dynamics of glider.

The laboratory glider designed in this study has a cylindrical hull with ellipsoidal nose and tail shapes, fixed wings and a tail fin [22]. In this model, the forces are resolved into axial and normal forces. The origin of E-frame is usually taken at the free surface so that Z is the depth. Equations of motion are defined in B-frame. CB is located at the centre of the ellipsoidal hull (origin of B-frame). The CG is located slightly offset from CB along axial direction to create a constant gravitational moment. In reference to E-frame, the velocity of the glider along x , y and z -axis is represented by u , v and w respectively while the angular velocity of the glider along x , y and z -axis is represented by p , q and s , respectively, all in B-frame. In B-frame, the position of the glider is represented by x , y and z along x , y and z -axis with reference to E-frame. The force balance relationship of a glider is shown in Fig. 1. In this figure, θ is the pitch angle (angle between X-axis

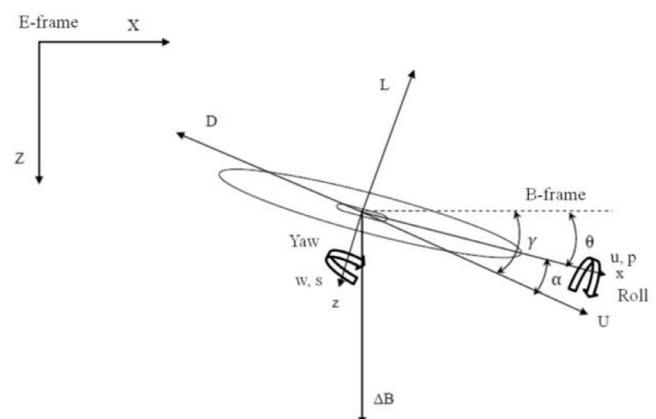


Fig. 1. Kinematic model of the glider.

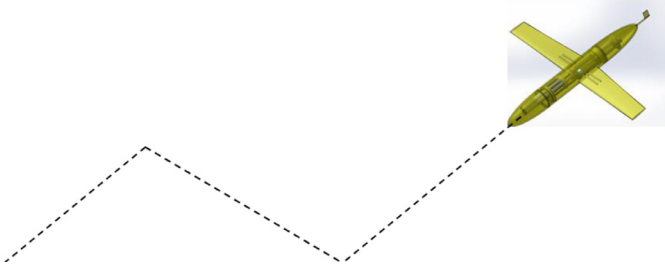


Fig. 2. Saw tooth glide trajectory (Source : [1]).

of E-frame and x -axis of B-frame), α is the angle of attack (angle between gliding velocity vector and x -axis of B-frame), γ is the gliding angle (angle between gliding velocity vector and X -axis of E-frame), U is the gliding velocity, L and D are vehicle lift and drag, respectively. When gliding down, γ and θ are positive and α is negative. When gliding up, γ and θ are negative and α is positive.

In real-time operations, all gliders are subjected to side forces due to underwater current which make glider move in a spiral trajectory, rather than the sawtooth trajectory as considered in this study. This spiral motion is used to change the direction of the glider movement underwater [31]. This work considers two-dimensional simulation and hence cannot consider the side forces and as a result the spiral steady state trajectory, which is a three-dimensional trajectory, cannot be obtained. In our study, the glider travels in an x - z longitudinal plane with no lateral movement. As a result, hydrodynamic effects of side forces are not considered. This travel results in a sawtooth trajectory of the glider as shown in Fig. 2.

The mass configuration of a glider is critical since it changes its mass while ascending or descending in water. The total mass of glider (m) consists of mass of the hull (m_h), internal moving point mass (m_m) and ballast mass (m_b). The component m_h includes the mass of variable buoyancy engine excluding the internal moving mass, mass of the wings and mass of the rudder. In commercial gliders such as Seaglider, m_m consists of two components, namely, sliding moving mass to control pitch and rotating moving mass to control roll. However, present laboratory glider is designed with only sliding moving mass. The ballast mass m_b of the glider is the mass of fluid taken in during its descent and given out during its ascent. Therefore, the total mass is

$$m = m_h + m_m \pm m_b \quad (1)$$

and the glider buoyancy (B) is given by

$$B = \rho g V \quad (2)$$

where ρ and V are the density of water and the volume of the glider, respectively. The net buoyancy (ΔB) can be defined as:

$$\Delta B = mg - B \quad (3)$$

If $m = B$, then glider is neutrally buoyant. The glider descends if $m > B$ (i.e. $\Delta B > 0$) and ascends if $m < B$ (i.e. $\Delta B < 0$). In order to maintain a steady glide, the state variables of glider (i.e. its velocity, gliding angle and angle of

attack) must remain constant. The kinematic and equilibrium relations follow from Fig. 2 [8] as:

$$\theta = \gamma - \alpha; \quad \Delta B \cos \gamma = -L; \quad \Delta B \sin \gamma = -D \quad (4)$$

The hydrodynamic drag and lift can be defined as:

$$D = -(K_{D0} + K_D \alpha^2) U^2 = -\frac{1}{2} C_D \rho S U^2$$

$$L = (K_{L0} + K_L \alpha) U^2 = \frac{1}{2} C_L \rho S U^2 \quad (5)$$

where K_{D0} and K_D are the zero (angle of attack) drag coefficient and induced drag coefficient respectively, K_{L0} and K_L are the zero (angle of attack) lift coefficient and induced lift coefficient respectively, C_D is the non-dimensional drag coefficient, C_L is the non-dimensional lift coefficient and S is the wetted surface area of the glider.

Eqs. (4) and (5) can be used to define the relation between α and γ as:

$$\tan \gamma = \frac{D}{L} = -\frac{(K_{D0} + K_D \alpha^2)}{(K_{L0} + K_L \alpha)}$$

or,

$$K_D \alpha^2 + K_L \tan \gamma \alpha + K_{D0} + K_{L0} \tan \gamma = 0 \quad (6)$$

For real and positive roots of the above quadratic equation one must have

$$(K_L \tan \gamma)^2 - 4K_D(K_{D0} + K_{L0} \tan \gamma) \geq 0 \quad (7)$$

Again for above quadratic equation, the roots can be represented as:

$$\tan \gamma = \frac{2K_D}{K_L} \left(\frac{K_{L0}}{K_L} \pm \sqrt{\left(\frac{K_{L0}}{K_L}\right)^2 + \frac{K_{D0}}{K_D}} \right) \quad (8)$$

Since values of $\tan \gamma$ lies between $-\infty$ and $+\infty$, hence the attainable value range of the gliding angle for a glider is:

$$\gamma = \left[-\frac{\pi}{2}, \tan^{-1} \left(\frac{2K_D}{K_L} \left(\frac{K_{L0}}{K_L} - \sqrt{\left(\frac{K_{L0}}{K_L}\right)^2 + \frac{K_{D0}}{K_D}} \right) \right) \right] \cup \left[\tan^{-1} \left(\frac{2K_D}{K_L} \left(\frac{K_{L0}}{K_L} + \sqrt{\left(\frac{K_{L0}}{K_L}\right)^2 + \frac{K_{D0}}{K_D}} \right) \right), \frac{\pi}{2} \right] \quad (9)$$

Eq. (6) is used to define the relation between α and γ as

$$\alpha(\gamma) = \frac{-K_L \tan \gamma}{2K_D} \left(1 \pm \sqrt{1 - \frac{4K_D \cot \gamma (K_{D0} \cot \gamma + K_{L0})}{K_L^2}} \right) \quad (10)$$

The gliding velocity can be expressed as a function of gliding angle using Eqs. (4) and (5) as follows:

$$\Delta B \cos \gamma = -(K_{L0} + K_L \alpha) U^2 \quad (11)$$

$$U = \sqrt{\frac{|\Delta B| \cos \gamma}{K_{L0} + K_L \alpha(\gamma)}} \quad (12)$$

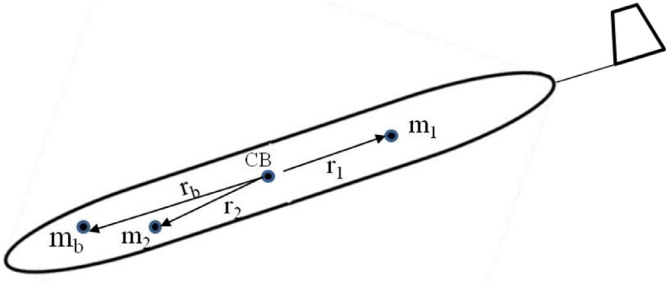


Fig. 3. Schematic representation of moving and ballast mass.

Substituting from $\alpha(\gamma)$, Eq. (10) in Eq. (12), one obtains

$$U = \sqrt{\frac{|\Delta B|2K_D}{2K_{L0}K_D \cos \gamma + K_L \sin \gamma (-K_L \pm \sqrt{K_L^2 - 4K_D K_{D0} \cot^2 \gamma - 4K_D K_{L0} \cot \gamma})}} \quad (13)$$

which is the relationship between the gliding velocity and the gliding angle for a specific driving buoyancy. Once we obtain γ from Eq. (8) that requires hydrodynamic coefficients alone, Eq. (13) can be solved for U and Eq. (10) will give the corresponding α . Then, the horizontal (U_H) and vertical (U_V) velocities are

$$\begin{aligned} \dot{X} &= U_H = U \cos(\theta + \alpha) \\ \dot{Z} &= U_V = U \sin(\theta + \alpha) \end{aligned} \quad (14)$$

2.2. Equations of motion of glider in vertical plane

Leonard and Graver [15] derived the equation of motions of glider in the vertical plane. These equations are simplified in accordance with our design configuration. Conventional glider design comprises of a sliding moving mass along the longitudinal axis to control pitch and rotary moving mass along the longitudinal axis to control roll. The major objective of such moving mass is to shift CG in forward and backward direction. In our design, there are two moving mass along with ballast mass which can move along the longitudinal axis whose schematic representation has been shown in Fig. 3. m_1 , m_2 and m_b denotes mass of the moving mass 1, moving mass 2 and ballast mass respectively, in the B-frame. The parameters, r_1 , r_2 and r_b represents the position of moving mass 1, moving mass 2 and ballast mass respectively, in the B-frame. P_1 , P_2 and P_b denotes momentum of the moving mass 1, moving mass 2 and ballast mass respectively, in the B-frame. B_e represents the position in E-frame while Ω and U represent the angular velocity vector and velocity vector in B-frame, respectively. R is the rotational matrix which defines the orientation of glider in B-frame and used for mapping of variables from B-frame to E-frame.

The control inputs to the system are the ballast rate (u_b), internal force (u_1) acting on the moving mass 1 and internal force (u_2) acting on the moving mass 2. u_{1x} and u_{2x} represent the internal force acting on moving mass 1 and moving mass 2 along x -direction. u_{1z} and u_{2z} represent the internal force acting on moving mass 1 and moving mass 2 along

z -direction. m_{fx} and m_{fz} represent the added mass along x and z -axis, respectively. K_{M0} and K_M are the zero moment coefficient and induced moment coefficient, respectively. I_{yy} represents the mass moment of inertia along y -axis. The detailed design is explained in the section five. The roll, yaw and sway velocity terms are taken to be zero. Assuming zero side-slip angles, the hydrodynamic shear force is neglected.

The simplified parameters for motion are expressed in Eq. (15) as:

$$\begin{aligned} B_e &= [x \quad 0 \quad z]^T; \quad \Omega = [0 \quad q \quad 0]^T; \quad U = [u \quad 0 \quad w]^T \\ r_1 &= [r_{1x} \quad 0 \quad r_{1z}]^T; \quad r_2 = [r_{2x} \quad 0 \quad r_{2z}]^T; \\ r_b &= [r_{bx} \quad 0 \quad 0]^T \\ P_1 &= [P_{1x} \quad 0 \quad P_{1z}]^T; \\ P_2 &= [P_{2x} \quad 0 \quad P_{2z}]^T; \quad P_b = [P_{bx} \quad 0 \quad P_{bz}]^T \\ u_1 &= [u_{1x} \quad 0 \quad u_{1z}]^T; \quad u_2 = [u_{2x} \quad 0 \quad u_{2z}]^T \end{aligned} \quad (15)$$

The velocity in B-frame can be expressed in E-frame as

$$\begin{bmatrix} \dot{x} \\ 0 \\ \dot{z} \end{bmatrix} = [R] \begin{bmatrix} u \\ 0 \\ w \end{bmatrix} \quad (16)$$

and the angular velocity in B-frame can be expressed in E-frame as:

$$\begin{bmatrix} 0 \\ \dot{\theta} \\ 0 \end{bmatrix} = [R] \begin{bmatrix} 0 \\ q \\ 0 \end{bmatrix} \quad (17)$$

where

$$[R] = \begin{bmatrix} \cos \theta & 0 & \sin \theta \\ 0 & 1 & 0 \\ -\sin \theta & 0 & \cos \theta \end{bmatrix}$$

The modified equations of motion are represented in Eq. (18) as:

$$\begin{aligned} \dot{x} &= u \cos \theta + w \sin \theta \\ \dot{z} &= -u \cos \theta + w \sin \theta \\ \alpha &= \tan^{-1} \frac{w}{u} \\ \dot{\theta} &= q \\ \dot{q} &= \frac{1}{I_{yy}} [(m_{fz} - m_{fx})uw - (r_{1x}P_{1x} + r_{2x}P_{2x} + r_{bx}P_{bx})q \\ &\quad - (r_{1z}P_{1z} + r_{2z}P_{2z})q - g \sin \theta (m_1 r_{1z} + m_2 r_{2z}) \\ &\quad - g \cos \theta (m_1 r_{1x} + m_2 r_{2x} + m_b r_{bx}) \\ &\quad + M_P - r_{1z}u_{1x} - r_{2z}u_{2x} + r_{1x}u_{1z} + r_{2x}u_{2z}] \\ \dot{u} &= \frac{1}{m_{fx}} [-m_{fz}wq - (P_{1z} + P_{2z} + P_{bz})q \\ &\quad - \Delta Bg \sin \theta + L \sin \alpha - D \cos \alpha - u_{1x} - u_{2x}] \\ \dot{w} &= \frac{1}{m_{fz}} [-m_{fx}uq - (P_{1x} + P_{2x} + P_{bx})q \\ &\quad + \Delta Bg \cos \theta - L \sin \alpha - D \cos \alpha - u_{1z} - u_{2z}] \\ \dot{r}_{1x} &= \frac{P_{1x}}{m_1} - u - r_{1z}q \end{aligned}$$

$$\begin{aligned}
\dot{r}_{1z} &= \frac{P_{1z}}{m_1} - w + r_{1x}q \\
\dot{r}_{2x} &= \frac{P_{2x}}{m_2} - u - r_{2z}q \\
\dot{r}_{2z} &= \frac{P_{2z}}{m_2} - w + r_{2x}q \\
\dot{P}_{1x} &= u_{1x} \\
\dot{P}_{1z} &= u_{1z} \\
\dot{P}_{2x} &= u_{2x} \\
\dot{P}_{2z} &= u_{2z} \\
\dot{m}_b &= u_b \\
P_{bx} &= m_b u \\
P_{bz} &= m_b (w - r_{bx} \Omega_2)
\end{aligned} \tag{18}$$

M_P represents the pitching moment and is modelled as:

$$M_P = (K_{M0} + K_M \alpha)(u^2 + w^2) \tag{19}$$

L and D are modelled as:

$$\begin{aligned}
L &= (K_{L0} + K_L \alpha)(u^2 + w^2) \\
D &= (K_{D0} + K_D \alpha^2)(u^2 + w^2)
\end{aligned} \tag{20}$$

U is denoted as:

$$U^2 = u^2 + w^2 \tag{21}$$

Graver [8] illustrated the use of the equations of motion to simulate the sawtooth gliding in the vertical plane by making use of the parameters of a glider similar in size as Slocum. This glider has one moving mass (m_1) which can slide along the longitudinal (i.e. x) axis and its x and z coordinates are denoted r_{1x} and r_{1z} , respectively. The control inputs to system were u_b , u_{1x} and u_{1z} . The parameters used for simulation are: $u_b = \pm 20$ g/s, $u_{1x} = \pm 0.02$ kg m/s², $u_{1z} = 0$, $K_{D0} = 2.15$, $K_D = 25$, $K_{M0} = 0$, $K_M = -100$, $K_{L0} = 0$, $K_L = 132.5$, $\Delta B = 47$ g, $r_{1x} = \pm 0.0198$ m, $r_{1z} = 0.05$ m, $m_1 = 9$ kg, $m_{fx} = 5$ kg, $m_{fz} = 70$ kg, $r_{bx} = 0$, $I_{yy} = 12$ kg m², $U_0 = 0.3$ m/s, $\theta_0 = \pm 23^\circ$

The first order coupled ordinary differential equations (ODEs) are solved using Runge–Kutta method. The results presented by Graver [8] are compared against our simulation to validate our simulation code and are shown in Fig. 4. All important parameters from our simulation are shown in Fig. 5.

In Fig. 5, U assumes non-zero values at $t=0$. This is due to the fact that simulation is subjected to initial velocity condition i.e. $U_0 = 0.3$ m/s. Ω_2 (i.e. q , the angular velocity) is a function of θ (pitch angle) in equations of motion. In the simulation, the pitch angle is subjected to initial conditions i.e. $\theta = \pm 23^\circ$. Hence, Ω_2 also has a non-zero value at $t=0$.

3. CFD analysis of an experimental glider

3.1. Selection of glider

The objective of this section is to establish a CFD methodology for the computation of the drag and lift forces on glid-

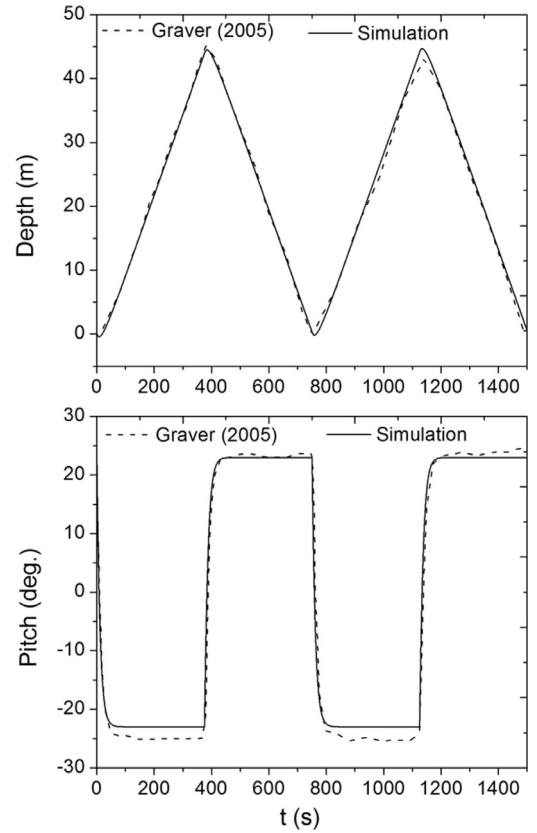


Fig. 4. Comparisons of pitch and depth.

ers. The behaviour of these forces gives the hydrodynamic coefficients of a glider that are required for its trajectory simulation. As a result, an accurate estimation of the hydrodynamic lift and drag forces is critical in studying glider trajectories under a variety of operating conditions. Since no experimental measurements of these hydrodynamic forces have been undertaken in the present work, it is important to validate the CFD methodology with experimental data. Towards this, a CFD validation exercise for an experimental glider, for which the drag and lift force measurements are reported in the literature, has been undertaken. The same CFD methodology is then used for the laboratory glider developed in the present work and these results are presented in the next section.

The hydrodynamic forces on a glider depend on the curvature of its forebody, afterbody and the wings. The wings provide the lift force that is required for the forward motion of the glider. In this chapter, an experimental glider, designated ‘Alex’ by Ichihashi et al. [12], has been considered for CFD analysis for estimating the drag and lift forces for various angles of attack and speed combinations. The design particulars of the Alex glider are presented in Table 1. The 3D CAD model of this glider and arrangement of the equipments inside are shown in Fig. 6. The drawing of the Alex showing dimensions, used for designing the model for present CFD analysis is shown in Fig. 7. An equivalent model as used by Ichihashi et al. [12] has been considered for CFD analysis.

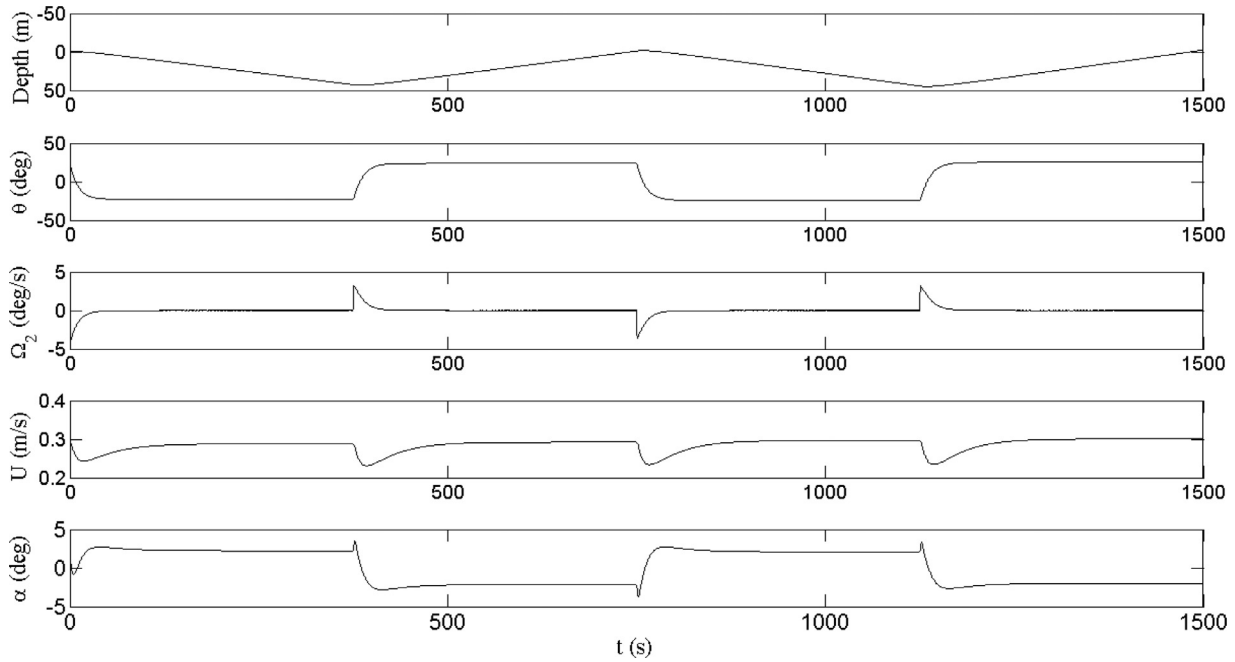


Fig. 5. Simulated parameters of the glider.

Table 1
Design particulars of the Alex glider [12].

Length	0.83 m
Breadth (wing span)	0.83 m
Height (including upper rudder)	0.17 m
Breadth of body	0.085 m
Mass	4.35 kg
Wing profile	NACA 0009
Wetted surface area (S)	0.4114 m ²
Wetted surface area (without rudder and wings)	0.3825 m ²
Cruising speed	0.2–1 m/s
Operation depth	5 m

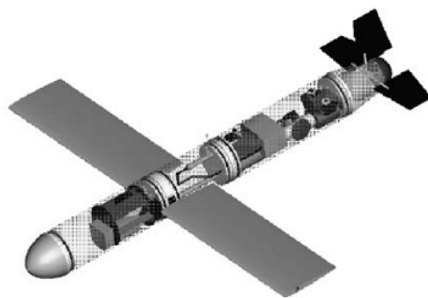
3.2. Towing tank test

Three component force measurements were carried out at the towing tank (Length × Breadth × Depth = 6 m × 1.5 m × 1 m) of Osaka Prefecture University. The lift and drag

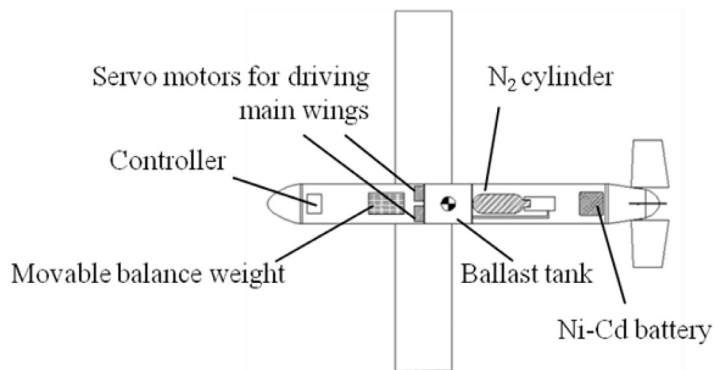
forces in the following two cases were measured for flow velocity (U) varying from 0.5 m/s to 0.8 m/s in steps of 0.1 m/s with (a) angle of the main wings (with the body) was at 0° and angle of attack of the body (α) was changed from −8° to 8° in steps of 2° and (b) angle of the body with respect to its velocity was at 0° and angle of the main wings with the body (β) was changed from −8° to 8° in steps of 2°. The arrangement of the experiment in the towing tank and directions of forces are shown in Fig. 8.

3.3. Computational domain and discretization

The computational domain ABEF around the experimental glider shown in Fig. 9 extends $L_f (= 1.3L)$ in the upstream of the leading edge of the body, $L_h (= 1.3L)$ in the radial direction (from the centerline of the body) and $L_a (= 5L)$ in the downstream of the trailing edge of the body, where



(a) 3D CAD model of Alex



(b) Internal arrangement of Alex

Fig. 6. Alex glider (from [12]).

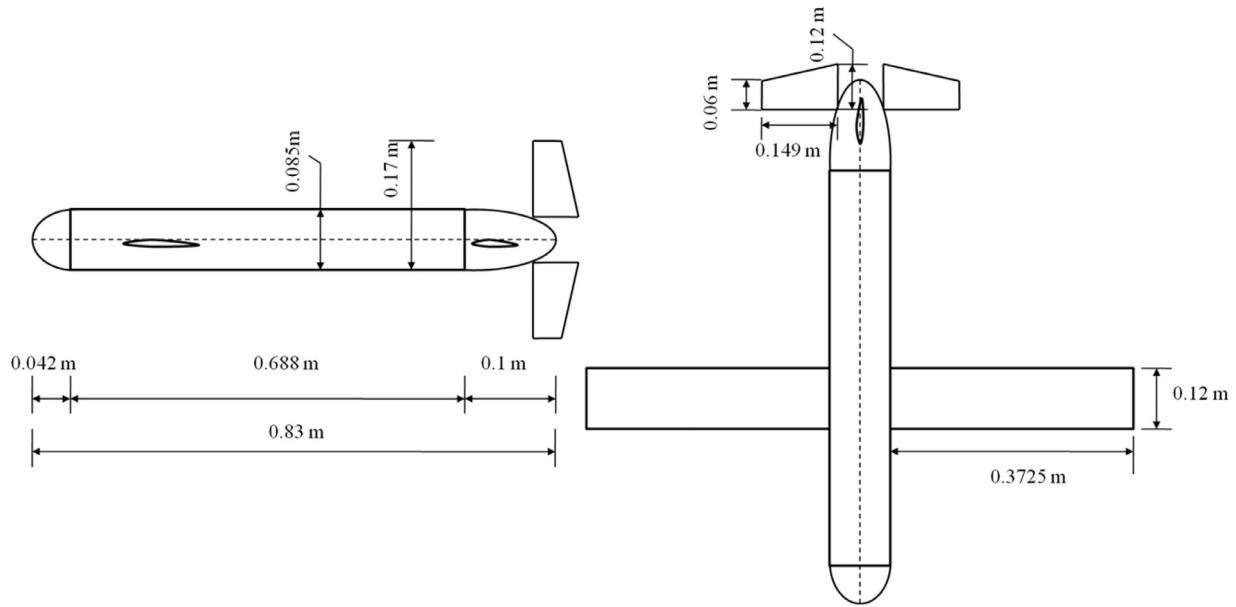
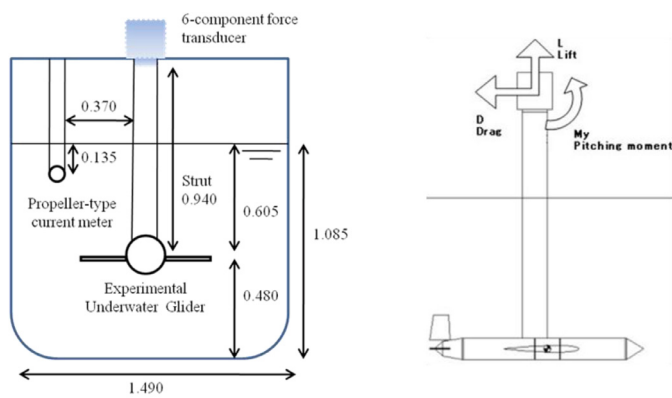


Fig. 7. Dimensions of Alex for designing model for CFD analysis.



(a) Arrangement of experiment (b) Direction of three component force in towing tank (dimension in m)

Fig. 8. Experimental setup for towing tank test (from [12]).

L is the length of the body. It also extends $1.3L$ in the z -direction. The domain extents are taken in accordance with ITTC [13] recommendations for marine CFD applications.

The domain around the body is discretized with the H-type structured grid. For computational efficiency and stability of the solution, the mesh should be such that it is dense in areas where the flow velocities are sensitive to grid spacing and coarse in other areas. The grid will be stretched towards no slip boundary conditions to get a y^+ (y -plus) value of approximately 1 for the first grid node adjacent to the body. The SST (shear stress transport) $k-\omega$ model is chosen for turbulence model, which is widely used in flow separation problems. For present analysis, a 2D axisymmetric grid of 101×60 and a 3D grid of $101 \times 60 \times 60$ has been used with a first grid point located at $y^+ < 1$. Fig 10(a) gives a view of the cells around the body in radial, axial and circumferential direction and Fig 10(b) shows the 3D domain and the mesh. Curvilinear O-grid is used to preserve the curvature of the body.

3.3.1. Boundary conditions

The physical state of the solution domain has been represented by a set of boundary conditions as shown in Fig. 10. In the implementation, two layers of ghost cells are used. The description of the mathematical conditions imposed at

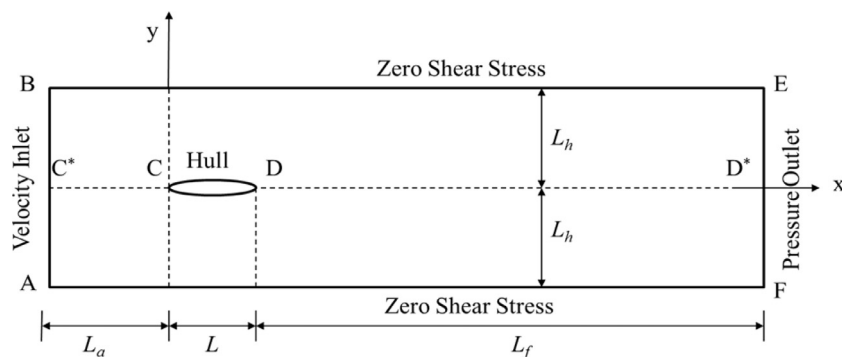


Fig. 9. Computational domain for glider with boundary conditions.

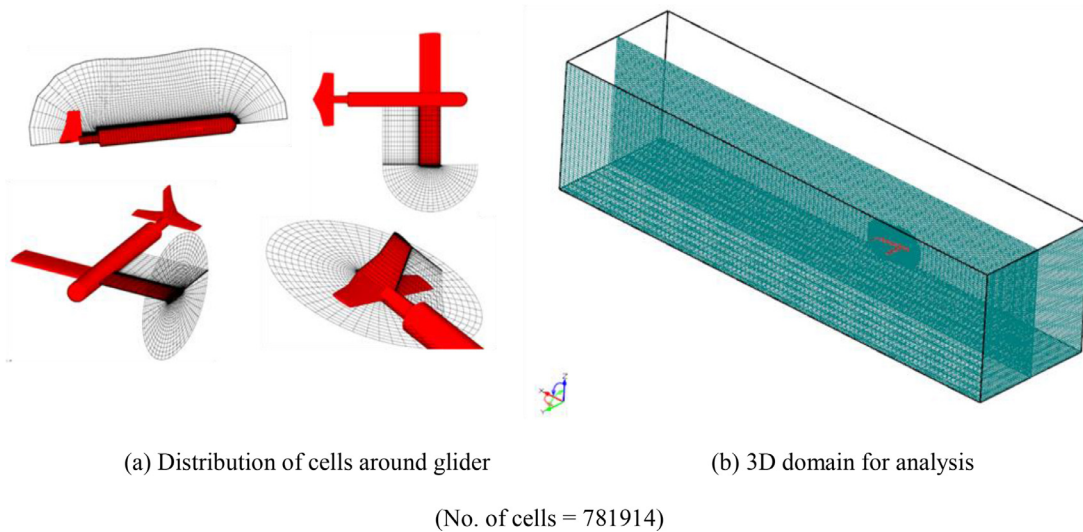


Fig. 10. Distribution of the cells around 3D model of the underwater glider.

Table 2
Boundary conditions [29].

	No slip (hull of vehicle-segment CD)	Slip (segment AF and BE)	Velocity inlet (segment AB)	Pressure outlet (segment EF)
u	$u_i = 0$	$u_i n_i = 0, \frac{\partial u_i}{\partial \xi_B} = 0$	$u_i = \text{constant}$	$\frac{\partial u}{\partial \xi_B} = 0$
P	$\frac{\partial P}{\partial \xi_B} = 0$	$\frac{\partial P}{\partial \xi_B} = 0$	$\frac{\partial P}{\partial \xi_B} = 0$	$P = 0$
k	$k = 0$	$\frac{\partial k}{\partial \xi_B} = 0$	$k = \text{constant}$	$\frac{\partial k}{\partial \xi_B} = 0$
ω	$\omega = f(u_r, \dots)$	$\frac{\partial \omega}{\partial \xi_B} = 0$	$\omega = \text{constant}$	$\frac{\partial \omega}{\partial \xi_B} = 0$

various physical locations in the domain has been described in Table 2.

In the above table, u_i represent time average velocity components in Cartesian directions, n_i represent normal to surface, ξ_B represent parameter direction crossing the boundary, k represent turbulent kinetic energy, ω represent specific dissipation of turbulent kinetic energy and P represent time average pressure.

3.3.2. Solver parameters

Commercial CFD solver SHIPFLOW 5.1.0 has been used to solve the steady state Reynolds averaged Navier Stokes (RANS) equations. The convective terms are discretized with a Roe scheme and a second order explicit defect correction is used to approach second order accuracy. The rest of the terms are discretized with central differences. A local artificial time-step is added to the equations and the discrete coupled equations are solved using an Alternating Direction Implicit (ADI)-solver. ADI is used to solve the equations. The tri-diagonal systems that are solved contains the first-order Roe convective terms and the second order diffusive terms, while the second-order flux corrections are used as an explicit defect correction. Each element in the tri-diagonal matrix is a 6×6 matrix. For each sweep, a local artificial time-step is calculated based on the Courant–Friedrichs–Lewy (CFL) and von Neumann numbers in all directions except the implicit one. The convergence is decided by the standard deviation of the viscous pressure resistance coefficient and frictional resistance

coefficient displayed in per cent of the average force. The convergence criterion in the present study is set as 1% for the viscous pressure resistance coefficient and frictional resistance coefficient. Computations are carried out until steady state is reached.

3.4. Validation of drag and lift forces using CFD

For four glider velocities (0.5, 0.6, 0.7 and 0.8 m/s) and nine angles of attack (-8° to 8° in steps of 2°), the drag and lift coefficients are computed using CFD are compared with the experimental as well as CFD results presented in Ichihashi et al. [12] in Figs. 11 and 12, respectively. For same four glider velocities and nine wing angles (-8° to 8° in steps of 2°), the drag and lift coefficients computed using CFD are compared with the experimental as well as CFD results presented in Ichihashi et al. [12] in Figs. 13 and 14, respectively.

These results show that whereas the lift coefficient matches well with CFD results of Ichihashi et al. [12] as well as the present work, the drag coefficient shows significant differences with both CFD results of Ichihashi et al. [12] as well as the present work. The CFD results of Ichihashi et al. [12] always over-predict drag by a large margin. On the other hand, the CFD results of the present work mostly under predict drag but yield a far superior match with experiments.

The CFD results of present work are closer to experimental values compared to those by Ichihashi et al. [12]. The reason

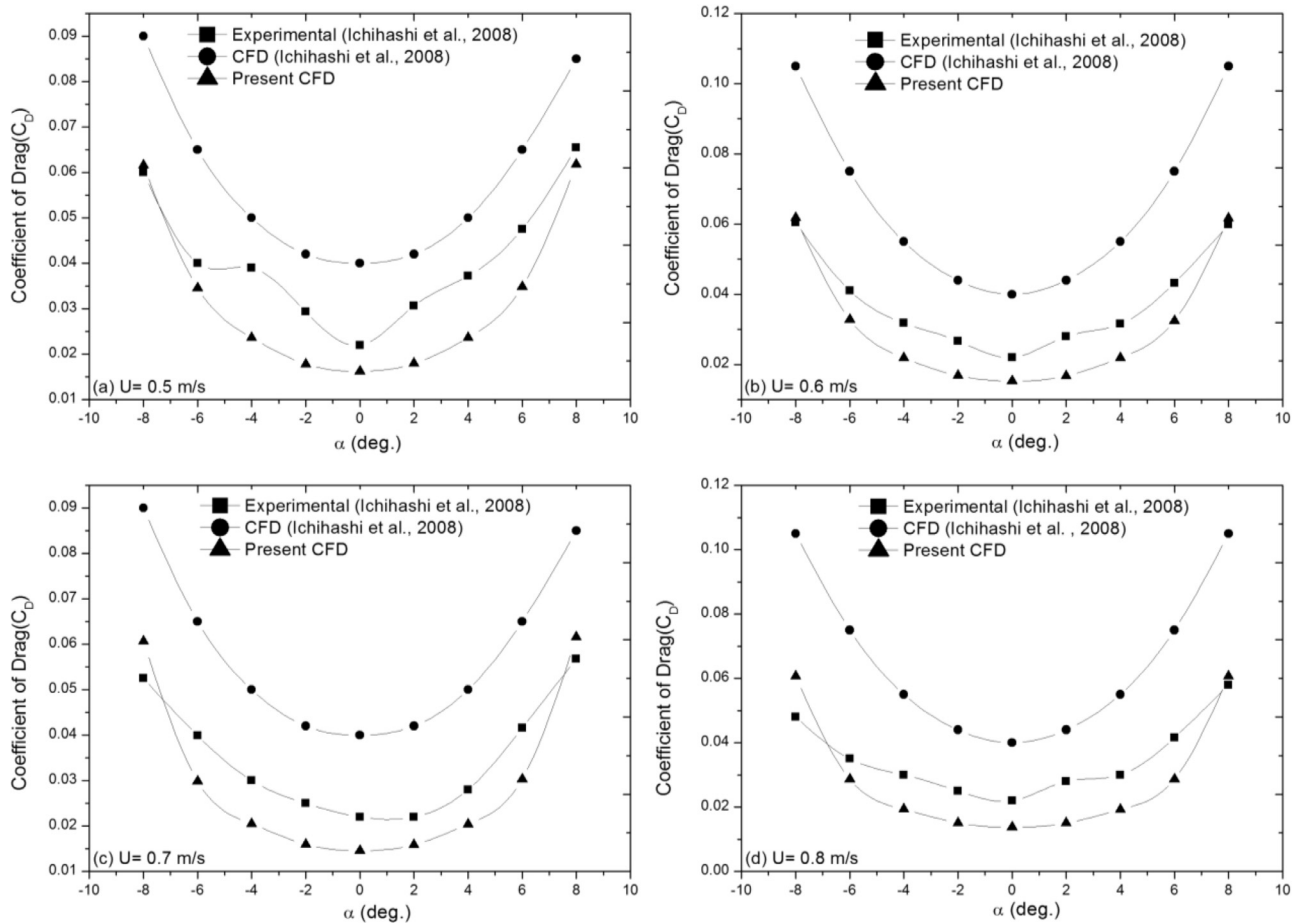


Fig. 11. Comparison of drag coefficient as function of angle of attack: CFD vs. experiments.

of this could be the use of the SST (shear stress transport) $k-\omega$ turbulence model in the present work, which is a preferred scheme to compute CFD results for applications having flow separation, instead of the $k-\varepsilon$ turbulence model used by Ichihashi et al. [12]. Clearly, more work in this area is warranted, but nevertheless the CFD approach can be adopted with confidence in predicting the hydrodynamic forces on gliders. Tables 3 and 4 describe the drag and lift comparison between experiment and CFD for $\alpha = -6^\circ$ respectively while Tables 5 and 6 describe the drag and lift comparison between experiment and CFD for $\beta = -6^\circ$, respectively.

4. CFD approach to steady state motion of glider

In this section, a detailed CFD analysis is carried out to obtain the hydrodynamic characteristics of the laboratory glider with symmetric wing profile that had been developed in the present work. Also, the results of simulation of steady state gliding motion making use of the CFD generated data are presented and discussed.

4.1. CFD analysis of laboratory glider

CFD analysis is performed to obtain the hydrodynamic coefficients, flow behaviour, force distribution and pressure

distribution on the glider surface for five glider velocities, ($U = 0.1, 0.2, 0.3, 0.4,$ and 0.5 m/s) and eleven values of angle of attack ($\alpha = -10^\circ$ to 10° in steps of 2°) for NACA 0012 wing configuration at $\beta = 0^\circ$. Flow is considered steady and incompressible.

4.1.1. Details of laboratory glider

The hull comprises of a nose section, cylindrical mid-section and a tail section. The nose and tail profiles are semi-ellipses with $a = 0.3$ m and $b = 0.07$ m for the nose profile and $a = 0.33$ m and $b = 0.07$ m for the tail profile, where a and b are the semi-major axis and semi-minor axis, respectively. The schematic drawing of the design is shown in Fig. 15 and its main design particulars are given in Table 7. The CFD grid and computational domain around the glider is shown in Fig. 16.

4.1.2. Effect of α on lift, drag and pitching moment coefficients

Fig. 17 shows the effect of α on the lift, drag and pitching moment coefficients of the laboratory glider. The definitions of these coefficients are:

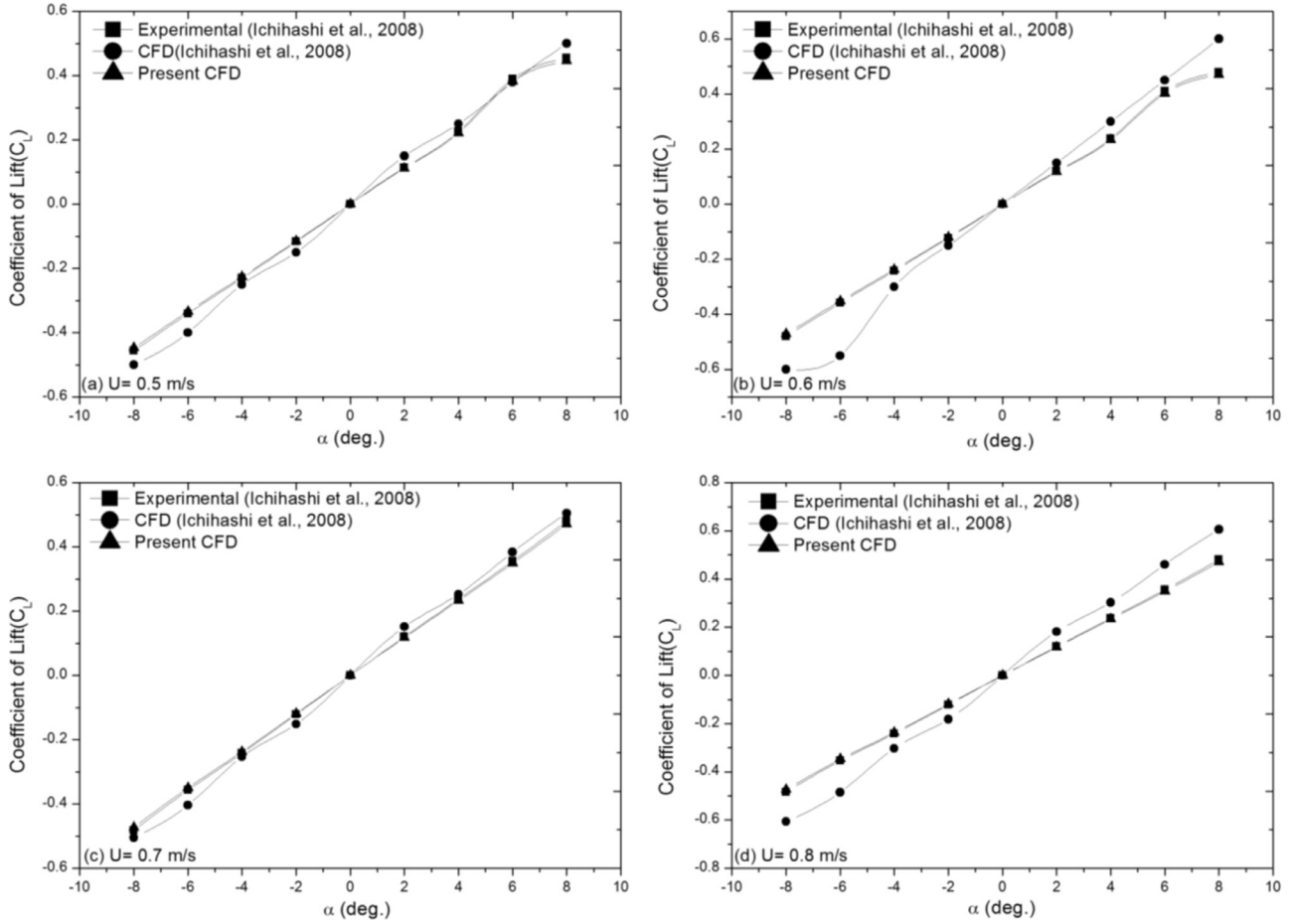


Fig. 12. Comparison of lift coefficient as function of angle of attack: CFD vs. experiments.

$$C_D = \frac{D}{\frac{1}{2}\rho S U^2} = K_{D0} + K_D \alpha^2$$

$$C_L = \frac{L}{\frac{1}{2}\rho S U^2} = K_{L0} + K_L \alpha$$

$$C_M = \frac{M}{\frac{1}{2}\rho S U^2} = K_{M0} + K_M \alpha \quad (22)$$

where L , D and M represent the total drag, total lift and total pitching moment that act on the glider respectively. C_D , C_L and C_M represent the drag, lift and pitching moment coefficients, S is the surface area of the glider.

Higher lift to drag (L/D) ratio is desirable for a glider. A comparative study has been carried out using CFD for a NACA0012 symmetrical wing profile and a NACA2315 cambered wing profile and the results are presented in Fig. 18. These results show that the maximum L/D ratios is about 8 at $\alpha = 6^\circ$ for NACA0012 and is about 6 at $\alpha = -6^\circ$ for NACA2315. This shows that the chosen symmetrical wing profile performs better than the chosen cambered wing profile. Therefore, NACA0012 profile is adopted for the laboratory glider. The predicted value of $L/D \approx 8$ is considered sufficiently high.

4.1.3. Static pressure distributions

Fig. 19 shows the static pressure distribution over the surface of laboratory glider in terms of pressure coefficient (C_p) whose definition is:

$$C_p = \frac{P_t}{\frac{1}{2}\rho U^2} \quad (23)$$

where P_t represents the total pressure. At any orientation, the nose of the glider has the highest magnitude of static pressure. Lift force on the glider is dependent on pressure distribution on the surface of a lifting body. As α increases negatively, the pressure distribution on the top surface of the glider and main wings is higher and negative lift force is generated while as α increases positively, the pressure distribution on the bottom surface of the glider and main wings is higher and positive lift force is generated.

4.1.4. Lift and drag force distributions

Tables 8 and 9 shows the contributions of the hull, wings and the tail to the total drag and lift forces for $U = 0.1$ m/s, respectively. The contribution of the tail is insignificant. The lift is mainly contributed by the wings and drag is mainly contributed by the hull.

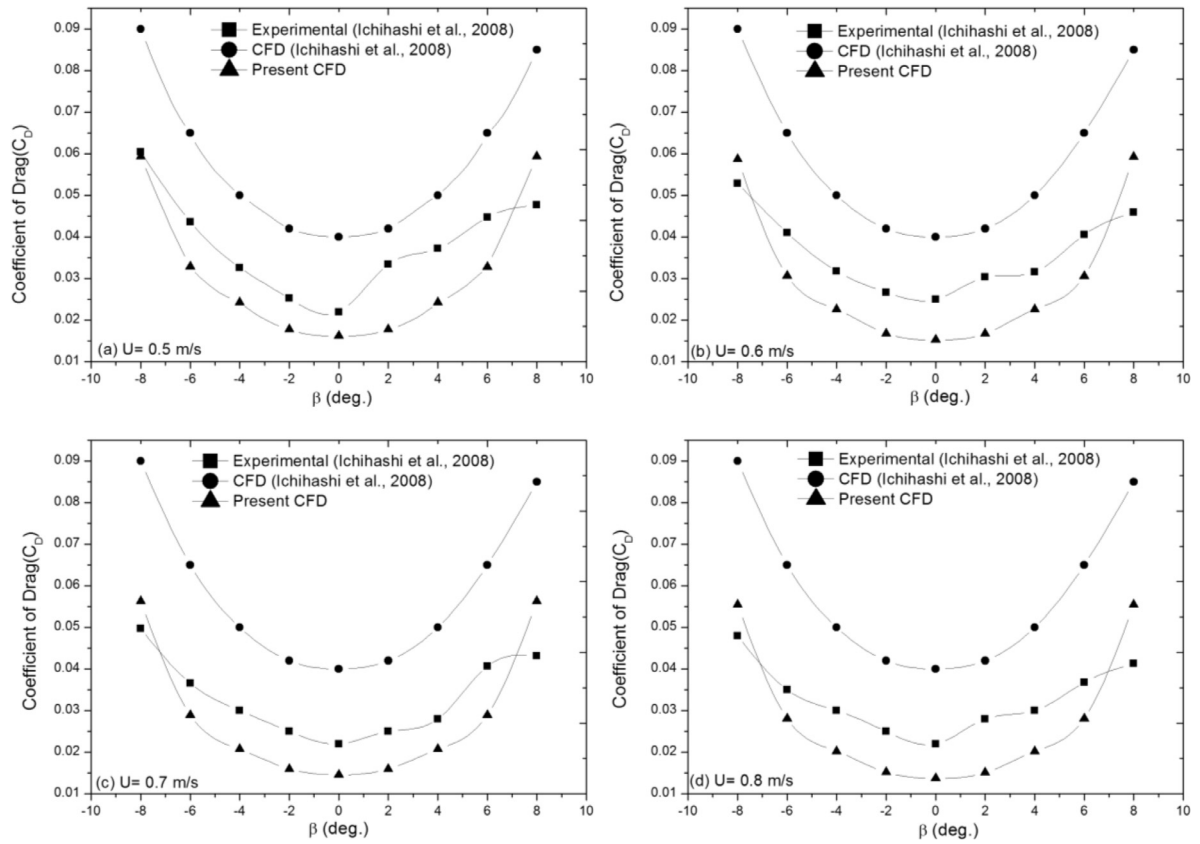


Fig. 13. Comparison of drag coefficient as function of wing angle: CFD vs. experiments.

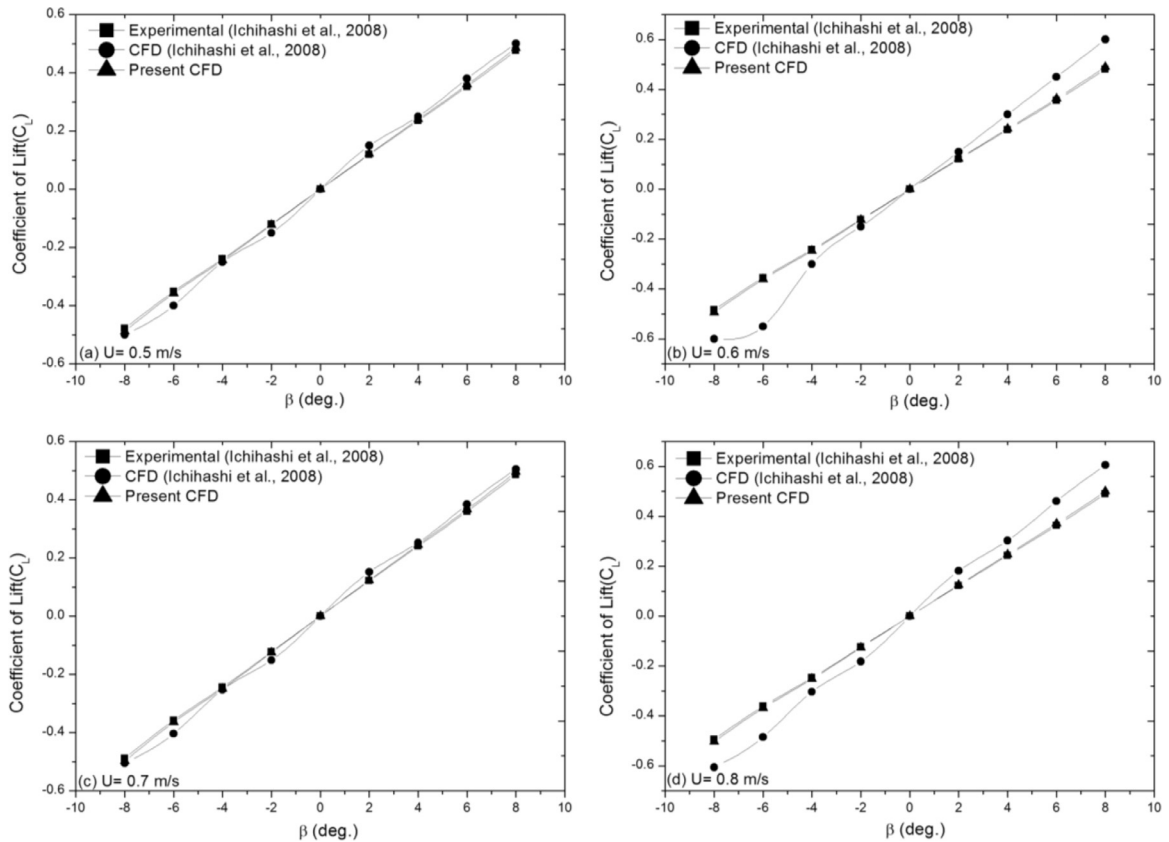


Fig. 14. Comparison of lift coefficient as function of wing angle: CFD vs. experiments.

Table 3
Comparison of drag coefficient (experiment vs. CFD) for $\alpha = -6^\circ$.

Velocity (m/s)	C_L experiment (1) [12]	C_L CFD (2) [12]	C_L CFD (3) (Present)	% difference (1) and (2)	% difference (1) and (3)
0.5	0.04	0.065	0.03459	-62.5	13.5
0.6	0.04104	0.075	0.03277	-82.7	20.15
0.7	0.03988	0.065	0.02982	-62.9	25.2
0.8	0.035	0.075	0.02864	-114.2	18.17

Table 4
Comparison of lift coefficient (experiment vs. CFD) for $\alpha = -6^\circ$.

Velocity (m/s)	C_L experiment (1) [12]	C_L CFD (2) [12]	C_L CFD (3) (Present)	% difference (1) and (2)	% difference (1) and (3)
0.5	-0.34067	-0.4	-0.33386	-17.4	1.9
0.6	-0.3586	-0.55	-0.35143	-53.3	1.9
0.7	-0.3572	-0.404	-0.35006	-11.58	2.0
0.8	-0.3544	-0.4848	-0.34731	-36.8	2.0

Table 5
Comparison of drag coefficient (experiment vs. CFD) for $\beta = -6^\circ$.

Velocity (m/s)	C_L experiment (1) [12]	C_L CFD (2) [12]	C_L CFD (3) (Present)	% difference (1) and (2)	% difference (1) and (3)
0.5	0.04366	0.065	0.03286	-48.8	24.7
0.6	0.04104	0.065	0.03066	-58.38	25.1
0.7	0.03655	0.065	0.02891	-77.8	20.1
0.8	0.035	0.065	0.02807	-85.7	19.8

Table 6
Comparison of lift coefficient (experiment vs. CFD) for $\beta = -6^\circ$.

Velocity (m/s)	C_L experiment (1) [12]	C_L CFD (2) [12]	C_L CFD (3)(Present)	% difference (1) and (2)	% difference (1) and (3)
0.5	-0.35086	-0.4	-0.35969	-14	-2.51
0.6	-0.3544	-0.55	-0.37149	-55.2	-2.69
0.7	-0.3572	-0.404	-0.36006	-13.1	-7.84
0.8	-0.36152	-0.4848	-0.36875	-33.58	-1.99

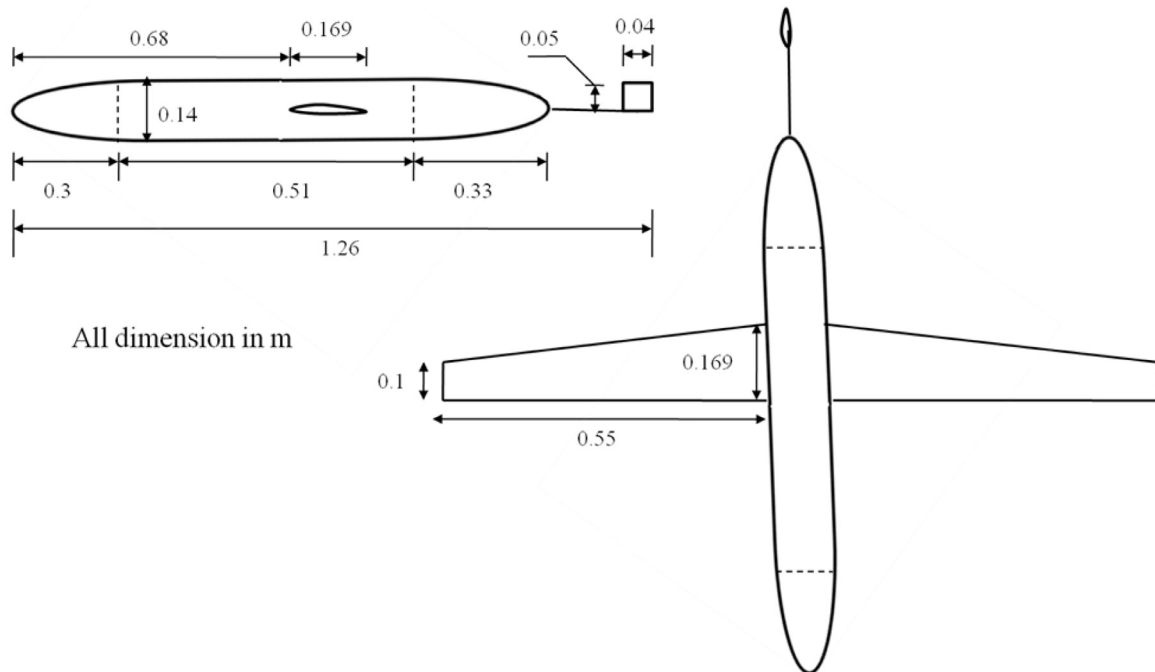
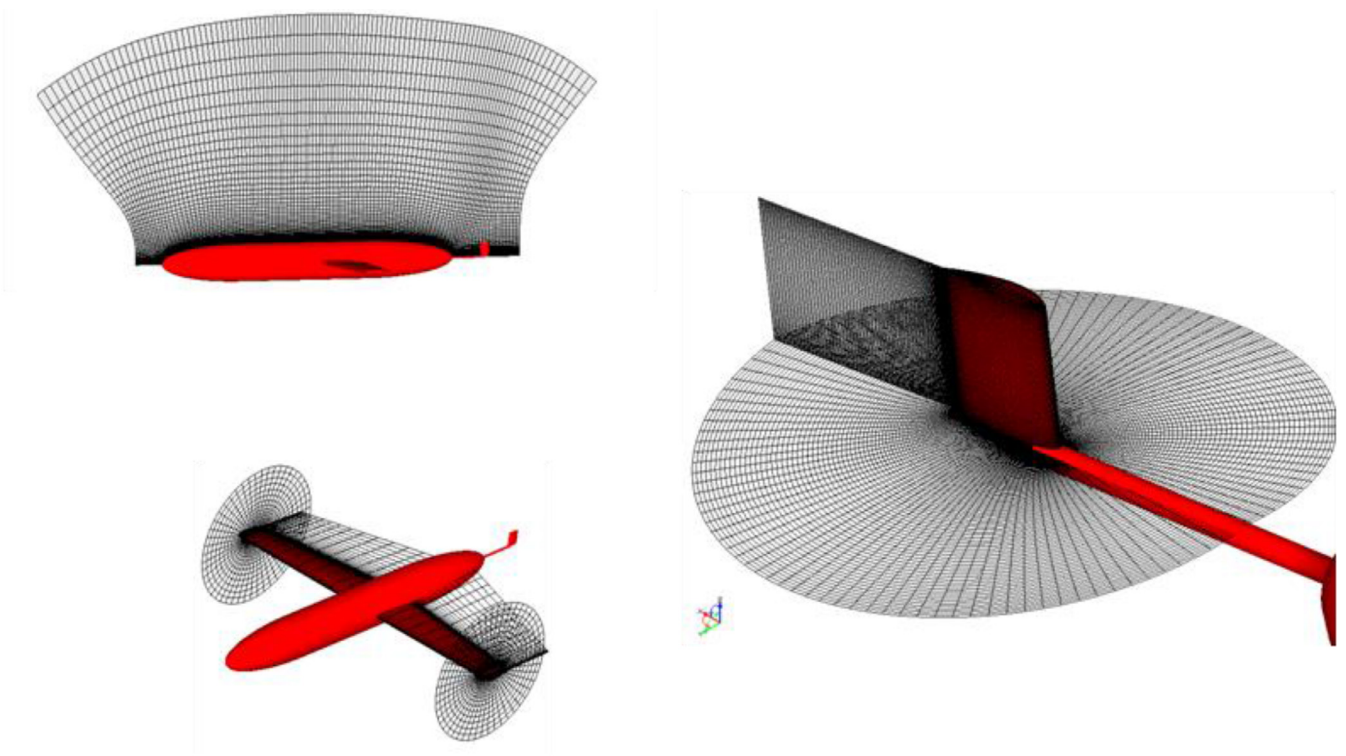
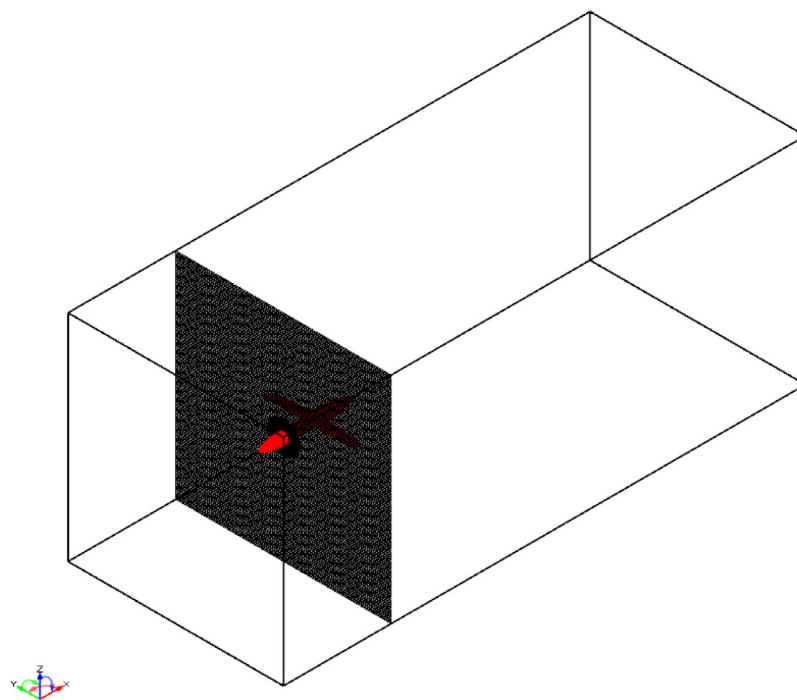


Fig. 15. Schematic drawing of laboratory glider.



(a) Structured grid around glider in radial, axial and circumferential directions (No. of cells = 1982726)



(b) 3D domain for laboratory scale glider

Fig. 16. 3D CFD model of the glider.

Table 7
Design particulars of laboratory glider.

Length	1.26 m
Wing span of each wing	0.55 m
Diameter	0.140 m
Wing and rudder profile	NACA0012
Wing chord	0.134 m (mean) 0.169 m (root) 0.1 m (tip)
Rudder chord	0.04 m
Rudder span	0.05 m
Operation depth	4 m
Wetted surface area (S)	0.7076 m ²
Wetted surface area without wings and rudder	0.4462 m ²

4.1.5. Velocity contours

Fig. 20 shows the velocity contours for glider at the symmetry plane. The velocity contour is represented by a non-dimensional velocity u_i/U , where u_i is the local flow velocity and U is the glider velocity. The area around the nose of the glider exhibits low velocity since the pressure is largest at this part. Wake is formed at the tail part of the glider. The wake is weak due to the low cruising speed of 0.1 m/s. As the α rises, the wake region expands. Fluid stream detaches itself from the glider at the rear region of the glider.

4.2. Steady state motion study

In this section, we present the results of the steady state motion simulation of the laboratory glider. The state variables of the glider are the velocity, gliding angle and angle of attack. These are simulated making use of drag and lift coefficient resulting in sawtooth trajectory of the glider. The effect of the variable buoyancy engine is examined in terms of state variables.

4.2.1. Identification of drag, lift and pitching moment coefficient

Eq. (22), which implies $C_D = K_{D0} + K_D\alpha^2$, $C_L = K_{L0} + K_L\alpha$ and $C_M = K_{M0} + K_M\alpha$ can be used to obtain the coefficients K_{D0} , K_D , K_{L0} , K_L , K_{M0} and K_M from the CFD generated data of C_D , C_L and C_M in Fig. 17 by polynomial fitting. Typical examples of this fitting are given in Fig. 21. The values obtained are $K_{D0} = 2.8304$ kg/m, $K_D = 0.02476$ kg/m, $K_{L0} = 0.03538$ kg/m, $K_L = 3.538$ kg/m, $K_{M0} = 0.014152$ kg/m and $K_M = 0.14152$ kg/m.

4.2.2. Simulation of state variables

The U as a function of pitching angle θ for three values of ΔB are shown in Fig. 22. The maximum U occurs at $\theta = 37^\circ$ for downward gliding (i.e. ΔB is negative) and at $\theta = -37^\circ$ for upward gliding (i.e. ΔB is positive) for all values of ΔB . The maximum values of U for $\Delta B = 0.3$ kg, 0.6 kg and 0.9 kg are 0.198 m/s, 0.281 m/s and 0.345 m/s respectively. The α as a function of θ and γ are shown in Fig. 23. In this figure, for $\theta = (37^\circ, -37^\circ)$, $\alpha = (-1.083^\circ, 1.062^\circ)$ and $\gamma = (35.917^\circ, -35.938^\circ)$.

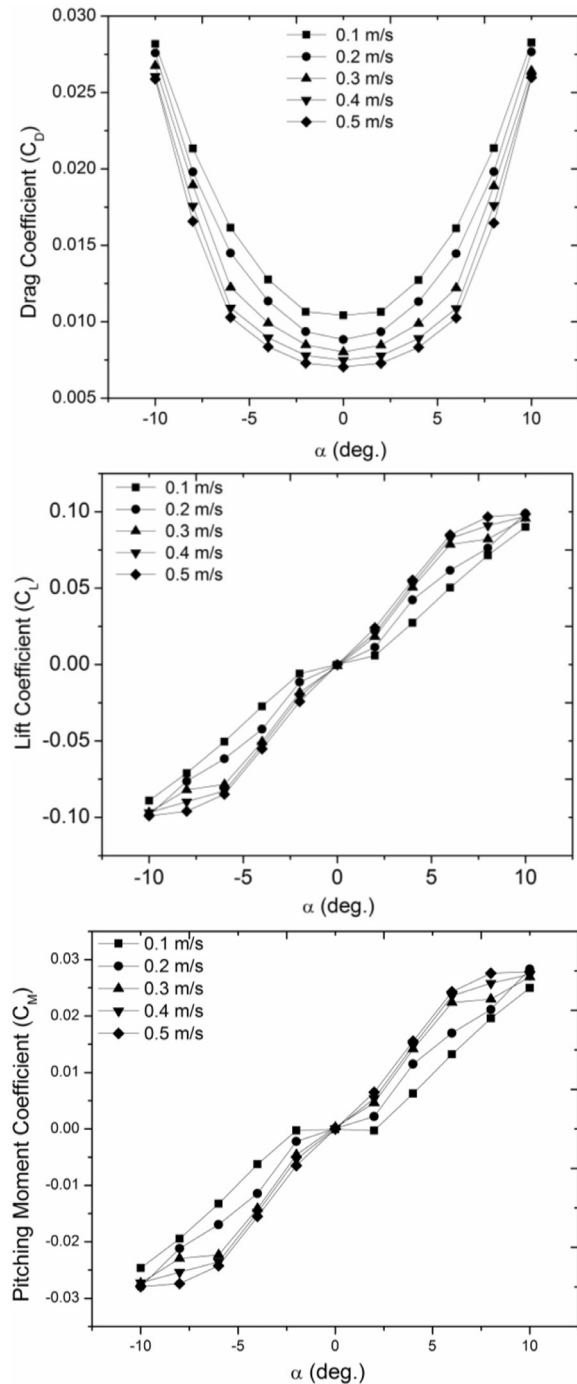


Fig. 17. Drag, lift and pitching moment coefficients with NACA 0012 wing profile using CFD.

From Fig. 24, it is seen that for 100 s simulation time the glider reaches the operational depth of 4 m in 33 s, 23.5 s and 19 s for $\Delta B = 0.3$ kg, 0.6 kg and 0.9 kg respectively and covers a horizontal distance of 15.4 m, 21.9 m and 26.9 m, respectively.

The performance of a laboratory glider with NACA0012 wing profile is studied using a CFD methodology. This profile gives a sufficiently high lift to drag ratio. The state variables of the glider are obtained from steady state simulation for

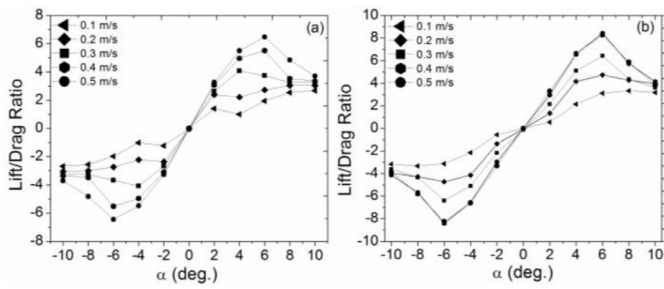


Fig. 18. Lift to drag ratio for (a) NACA2315 (b) NACA0012 wing profile.

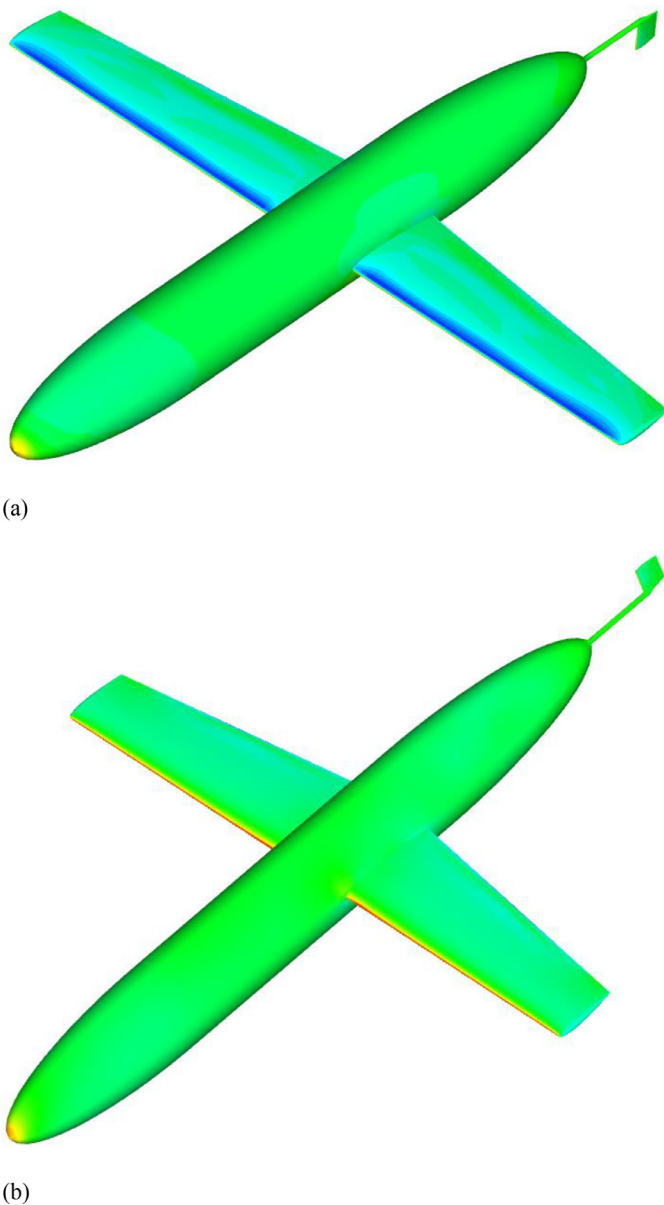


Fig. 19. Pressure distribution over (a) bottom and (b) top surface for $U=0.1$ m/s at $\alpha=-6^\circ$.

Table 8
Drag force distribution for $U=0.1$ m/s.

α	Drag (in %)			Drag (in N)
	Hull	Wings	Tail	
0°	65	35	0	0.03686
4°	69	30	1	0.04503
8°	72	27	1	0.07557
-4°	69	30	1	0.04514
-8°	70	28	2	0.07550

Table 9
Lift force distribution for $U=0.1$ m/s.

α	Lift (in %)			Lift (in N)
	Hull	Wings	Tail	
0°	–	–	–	0
4°	19	81	0	0.09669
8°	20	80	0	0.2527
-4°	19	81	0	-0.09679
-8°	20	80	0	-0.2514

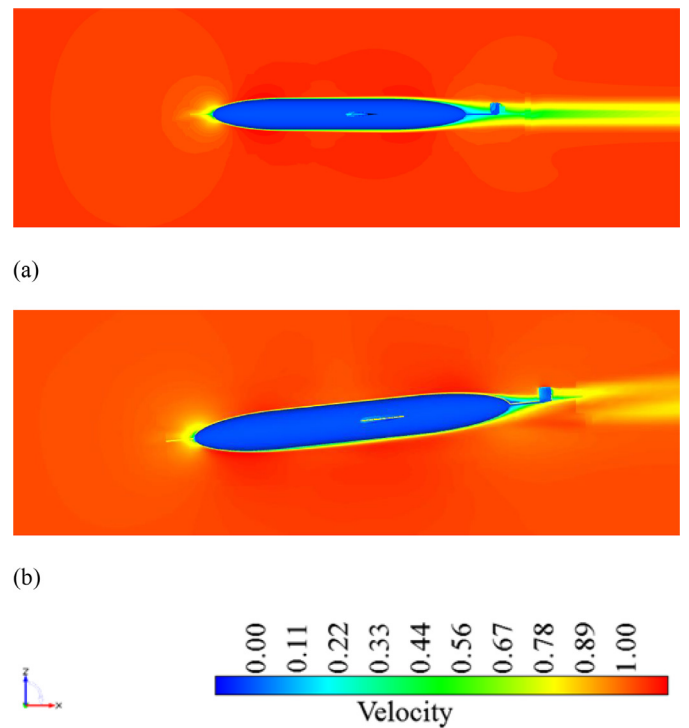


Fig. 20. Nondimensional velocity contours at (a) $\alpha=0^\circ$ (b) $\alpha=-6^\circ$ for $U=0.1$ m/s.

three values of ΔB and the glider trajectories obtained for a chosen operational depth. It was found that the glider with larger ΔB covers a larger horizontal distance and takes less time to reach the operational depth as a result of higher gliding velocity at same gliding angle and angle of attack. This suggests that a glider with a larger change in buoyancy is more efficient in operation and can achieve a longer range.

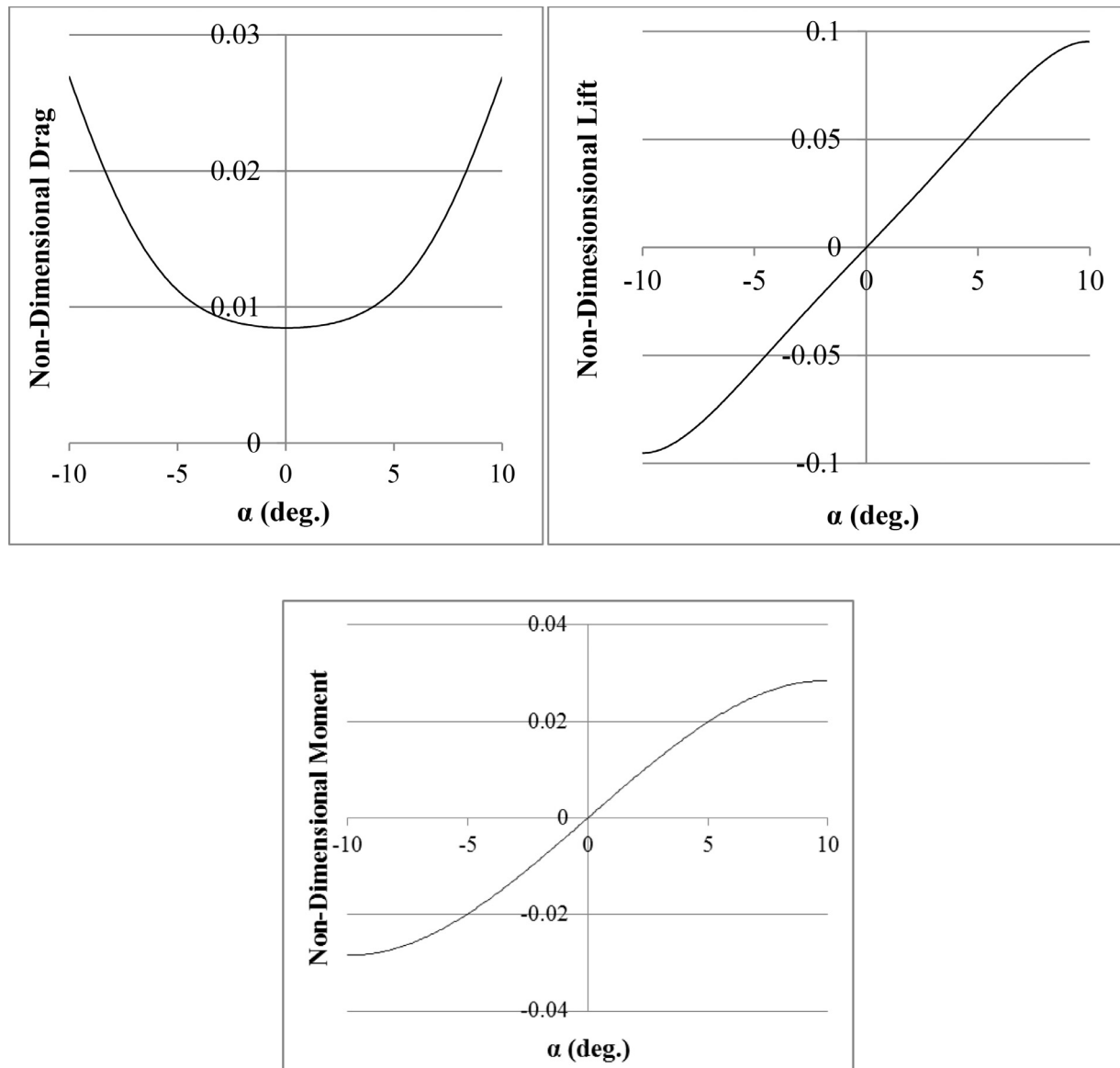


Fig. 21. Curve fitting of drag, lift and pitching moment.

5. Design and development of a laboratory glider

This section reports the effort that has been made to develop a low cost laboratory scale glider. The design and fabrication of a glider has been carried out and studied numerically as well as experimentally and the results compared. The CFD results of the glider had been discussed in previous section. In this section, we discuss the design details, fabrication of the glider, its variable buoyancy engine, wings and rudder.

5.1. Fabrication of the glider hull

The glider hull consists of three sections namely forward elliptical (spheroidal) section, middle cylindrical section and aft elliptical section and the rudder section. The major dimension of the different sections of glider hull is tabulated in Table 10 (also see Fig. 25).

Polyvinyl Chloride (PVC) is used to fabricate the mid section while the aft and forward sections are fabricated using Fibre Reinforced Plastic (FRP). Fig. 25 shows the CAD model of the hull sections and the fabricated hull sections. Aluminium rings are attached to the forward and aft hull sections to ensure a waterproof push fit with the mid section. The mid section is attached with aft and forward hull section through bolt. The wing profile of the glider is NACA0012 as discussed in previous section. Fig. 26 shows the profile of NACA0012 section.

The design details of the wing and rudder are given in Table 11. Fig. 27 shows the CAD model of the wings and the fabricated wings attached to the mid section of the hull. Screws and bolts are used to fix the wings with the mid section. Fig. 28 shows the CAD model of the rudder. The rudder is attached to the aft section using screw and nut arrangement.

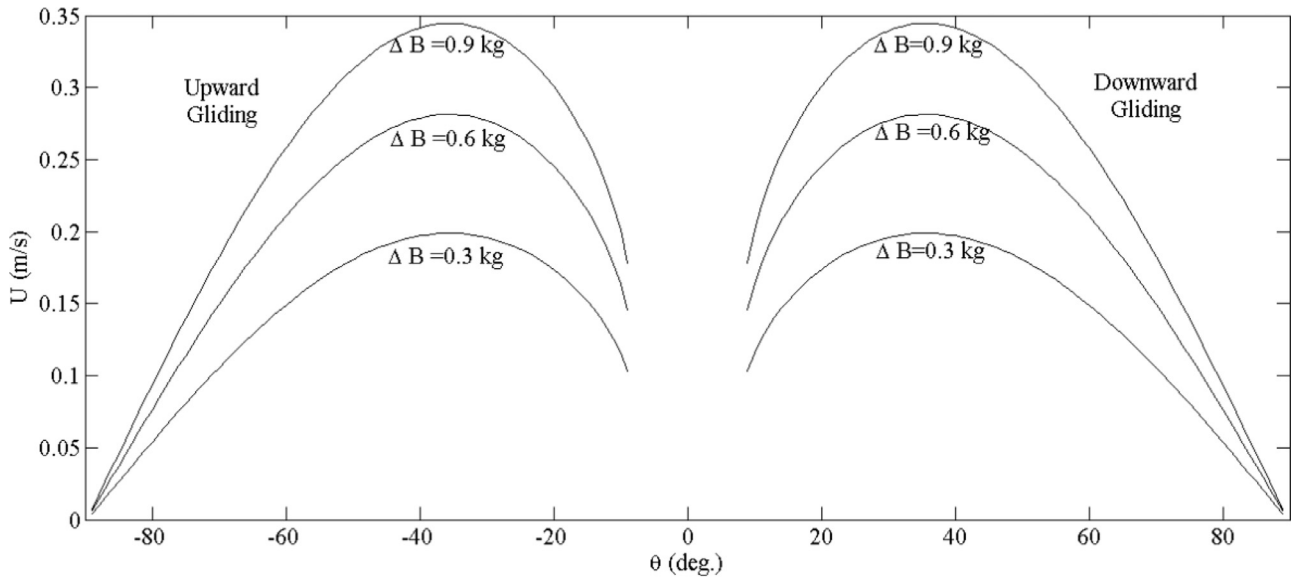


Fig. 22. Gliding velocity vs. pitching angle.

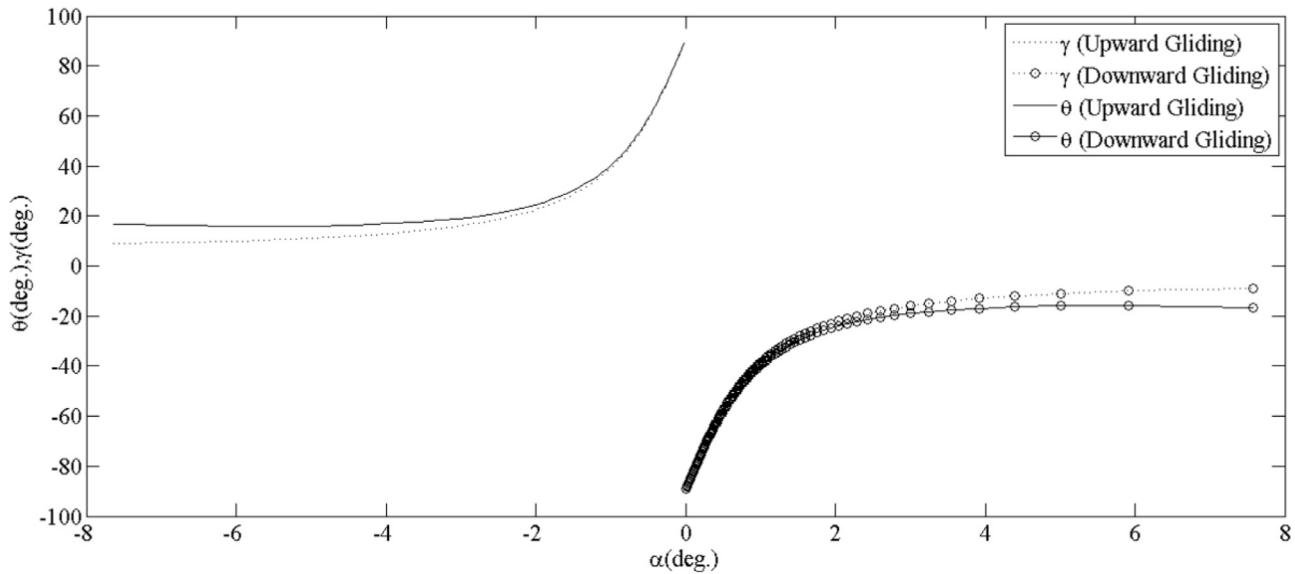


Fig. 23. Angle of attack vs. pitching angle.

5.2. Fabrication of the variable buoyancy engine

There are three main types of variable buoyancy (VB) engines used in underwater vehicles, namely, mass discharge system, pumped water system and oil displacement systems as stated by Harold [11]. Other than equipment upgrades and minor variations, there had been no major recent advancements in the technology.

The design requirements of a VB system for a laboratory glider are based on energy consumption for its pumping mechanism, speed of the pumping mechanism, discharge volume and depth of operation. In the present study, a discharge mass of 0.3 kg is enough to make glider glide for the specified operational depth of 4 m (see Table 7) using 12 V DC motor based pumping mechanism, based on tests con-

ducted and relations explained in Worall et al. [28] and Zhao et al. (2011) for the design of VB systems for deep ocean vehicles.

Taking into account the ease of manufacturing, hull design, availability of materials, test depth and cost of fabrication, a pumped water VB engine has been chosen in the present work. The VB engine for the glider is a piston cylinder based VB arrangement incorporated with a moving mass arrangement. Two high torque, 12 V DC motors connected with lead screws are used for the linear actuation of piston cylinder and moving mass arrangement. Specifications of the motor are given in Table 11.

The calculated torque required for the actuation of the piston cylinder arrangement was 90 kg cm. Hence, this motor suits the cost and torque requirement of the model.

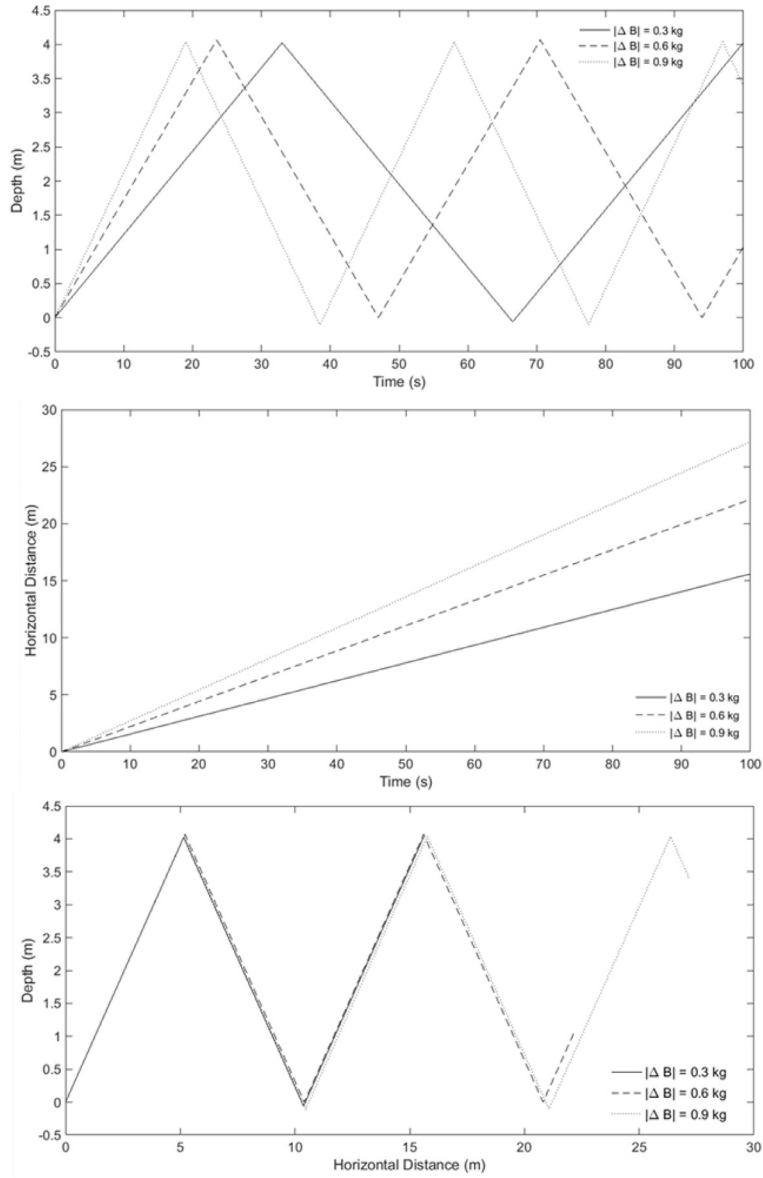


Fig. 24. Trajectories for three values of ΔB for upward and downward glider.

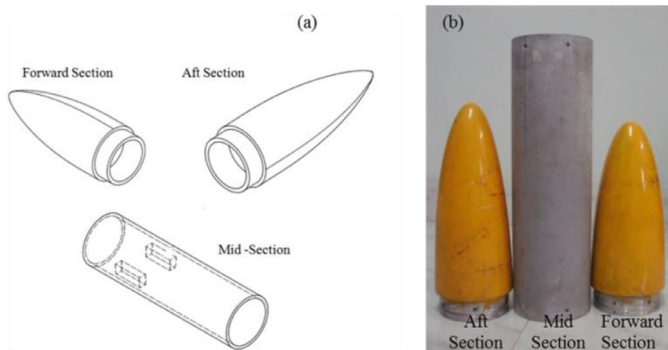


Fig. 25. (a) CAD model of hull sections (b) fabricated hull sections.

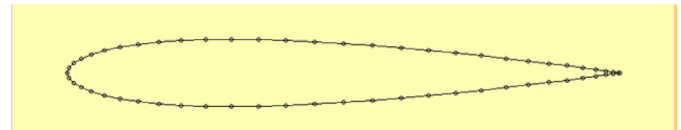


Fig. 26. 2D profile of NACA0012.

The motor assembly is connected to the main frame using two 12 mm diameter, 5 mm pitch MS lead screws connected with the shaft of both motors to convert the rotary motion of the shaft into a linear one. The CAD model of the main frame and its fabricated version is shown in Fig. 31.

Three buoyancy chambers made from acrylic tubes of 365 mm length are connected with the top lead screw as shown in Fig. 32(a) through piston rods. The bottom and top lead screws are connected with the moving mass 1 and

Fig. 29 shows the model and dimensions of the motor. The CAD model and fabricated model of the assembly of both motors within the VB setup has been shown in Fig. 30.

Table 10
Design particulars of the glider hull.

Particulars of section	Details
Forward section:	
Length	300 mm
Material	FRP (5 Layered)
Weight	1.78 kg
Mid section:	
Length	510 mm
Material	PVC (10 Gauge)
Weight	2.16 kg
Aft section:	
Length	330 mm
Material	FRP (5 Layered) 2.16 kg
Weight	
Length of glider (including rudder)	1260 mm
Outer diameter of mid section	140 mm (= d_b)
Inner diameter of mid section	124 mm

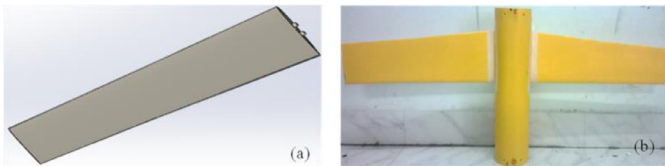


Fig. 27. (a) CAD model of wings (b) fabricated wings attached to the mid section.

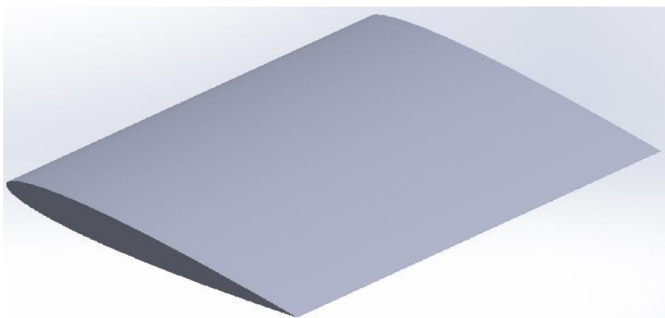


Fig. 28. CAD model of rudder.

Table 11
Specifications of DC motor.

RPM	10 at 12 V for moving mass, 60 at 12 V for piston
Voltage	4–12 V
Stall torque	106.08 kg cm at stall current of 4.4 A
Shaft diameter	8 mm
Shaft length	25–30 mm
Gear assembly	Spur
Brush type	Carbon
Motor weight	480 g

moving mass 2, respectively, whose details are given in Table 12. The fabricated model of the full VB engine is shown in Fig. 32(b).

Three circular slots encompassed with brass caps have been engraved in the nose part of the hull, connecting the acrylic buoyancy chamber through silicon tubes for suction and ejection of the surrounding water. The VB engine can

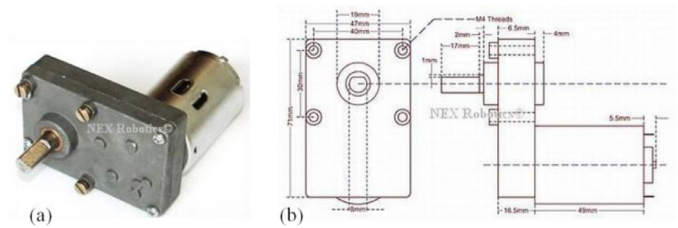


Fig. 29. (a) Motor model (b) dimension of the motor (source: NEX Robotics Website).

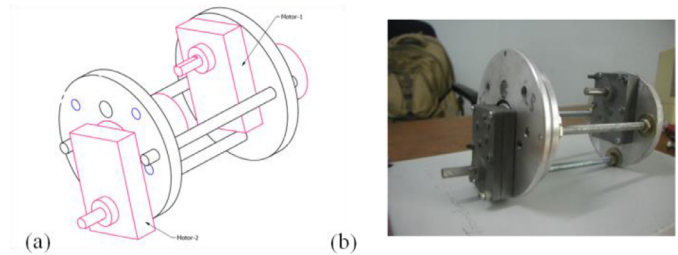


Fig. 30. (a) CAD model of motor assembly (b) fabricated model of motor assembly.

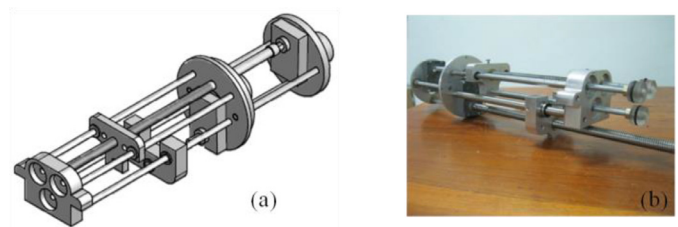


Fig. 31. (a) CAD model of mechanism assembly (b) fabricated model of mechanism assembly.

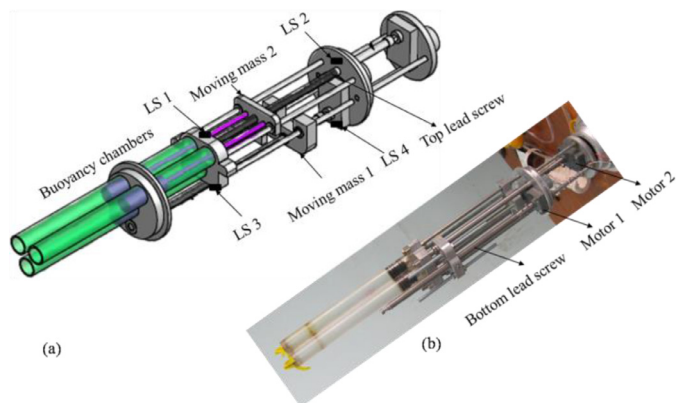


Fig. 32. (a) CAD model of VB engine (b) fabricated model of VB engine.

suck in and eject 0.3 kg of water from the surrounding. The frames used to mount motors, lead screws, moving mass mechanism and moving piston arrangement are made of H30 Aluminium.

5.3. Assembly of glider

After fabrication of the hull sections, wings, rudder and VB engine, both motors were connected to an external power

Table 12
Details of moving mass.

Moving mass 1	0.5 kg
Moving mass 2	0.18 kg
Total traverse of moving mass 1	25 cm
Total traverse of moving mass 2	20 cm

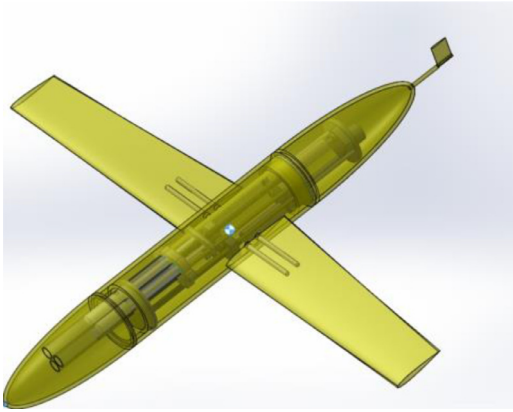


Fig. 33. Assembled view.

Table 13
Breakup of the mass of glider.

Component	Weight (in kg)
Forward section	1.78
Mid section	2.16
Aft section	2.16
VB engine (including moving mass)	5.85
Rudder section	0.1
Wings (each wing 0.72 kg)	1.44
Total	13.49

source through a remote, comprising of two switches to control the movement of two motors. To identify the extreme positions of piston rod and moving mass, four limit switches (namely LS 1 to LS 4) were placed on extreme ends of the bottom and top lead screw as shown in Fig. 32(a). The positions of moving masses within the glider hull are explained in subsequent section. After electrical connections were made, VB engine was placed within the hull sections and resin was applied to make the hull watertight along with nut and bolts. The assembled view of the glider is shown in Fig. 33.

5.4. Buoyancy adjustment

It is important for any buoyancy driven vehicle to ensure that a proper match between mass and buoyancy is maintained. The mass of the laboratory glider after assembly was found to be 13.49 kg, whose breakup is tabulated in Table 13.

The mass of the glider at full ballast condition was found to be 13.79 kg. The displaced mass of the glider was found to be 15.65 kg. Hence, it was required to add a dead weight of 1.9 kg so that the difference of 0.3 kg between the mass and buoyancy is maintained.

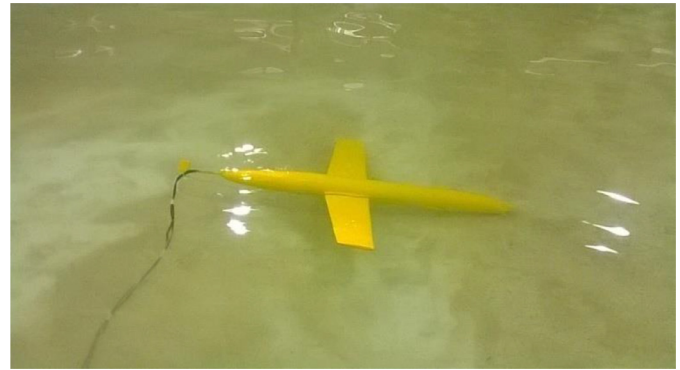


Fig. 34. Trim observed in initial test.

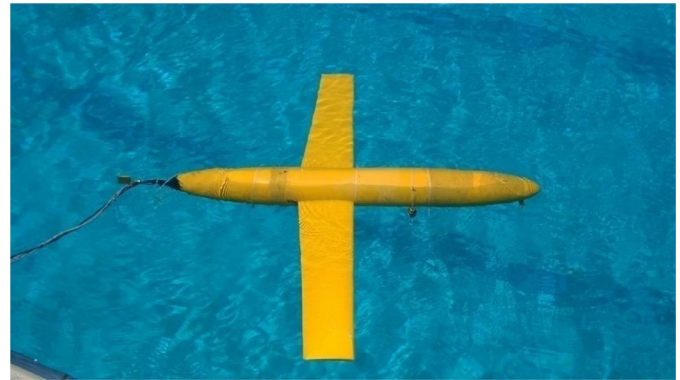


Fig. 35. Glider in zero trim condition at floating.

5.5. Trim adjustment

After assembling the laboratory glider, an initial test was conducted to determine its trim and also to check leakage if any. A trim was observed in this test as shown in Fig. 34.

Proper distribution of weight is important to maintain a zero (or negligible) trim of the glider during floatation. MS plates weighing 1.53 kg were added on the forward side while circular copper pieces weighing 0.37 kg were added on the aft side. After proper distribution of the deadweights, a zero trim was observed as shown in Fig. 35.

5.6. Sensors

To measure the performance of the laboratory glider in terms of depth profile, roll and pitch angles during its saw-tooth motion, two sensors, namely, pressure sensor and inclinometer were used. The specifications of pressure sensor and inclinometers are tabulated in Tables 14 and 15, respectively.

The pressure sensor was placed at the forward section of the glider hull while the inclinometer is placed on the aft section of the glider hull as shown in Fig. 36.

6. Experimental study of glider trajectory

In this section, the experimental validation of the trajectory of the laboratory glider in the vertical plane against the

Table 14
Specifications of pressure sensor.

Manufacturer	Honeywell Corporation (26 PCCFA6G)
Mass	0.002 kg
Operating pressure	± 0.10324 MPa
Operating supply voltage	10 V
Mounting style	Through hole
Accuracy	0.2 %
Output type	Analog
Pressure type	Vacuum, gauge




Table 15
Specifications of inclinometer.

Manufacturer	Posital Fraba
Mass	0.1 kg
Measurement range	±80° (dual axis)
Accuracy	0.1°
Resolution	0.01°
Analog interfaces	Current, voltage


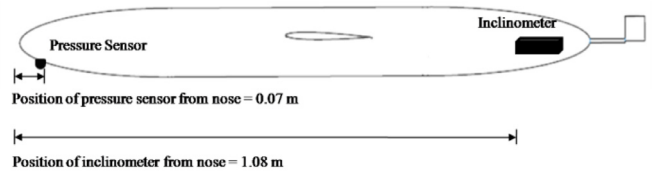



Fig. 36. Position of inclinometer and pressure sensor in glider hull.

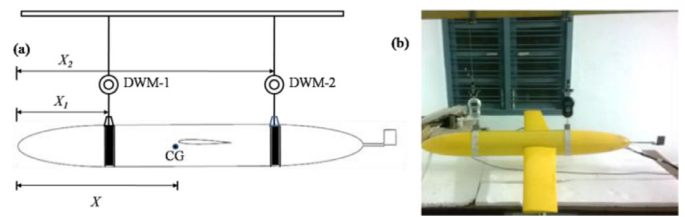


Fig. 37. Setup for CG test.

numerically computed trajectory using the equations of motion presented in previous section is presented. The hydrodynamic parameters that appear in these equations have been obtained from CFD results presented in previous section and other parameters (e.g. mass, mass moments of inertia, etc.) are obtained experimentally. Towards this, CG determination test, bifilar pendulum test and rolling pendulum test have been conducted. Deployment trials in wave flume and swimming pool at IIT Madras had been conducted to determine the roll, pitch and depth, i.e. the dynamic characteristics of the glider, as functions of time. Results of these trials give the trajectory of the glider in the vertical plane. It should, however, be noted that the laboratory glider is not ‘autonomous’ but has wire connection at its tail end through which signals to control the moving masses and buoyancy is carried out.

6.1. Static and oscillation test

6.1.1. CG determination

The CG position along the axial direction is determined by hanging the glider with two mild steel strings at known positions along the horizontal axis and readings are taken using a digital weighing machine (DWM). The schematic and actual setup is shown in Fig. 37. The CG of the glider can

be determined by

$$X = \frac{M_1 X_1 + M_2 X_2}{M_1 + M_2} \tag{24}$$

where X is distance of CG from the nose, X₁ and X₂ are the distances of DWM 1 and DWM 2 from the nose and M₁ and M₂ are the readings from DWM 1 and DWM 2, respectively.

The DWM is connected with the glider using steel clamp as shown in Fig. 37(b), each weighing 0.22 kg. The CG calculations have been made by taking into account the weight of each clamp during the test and validating the test value with the corresponding CAD model. The CG values have been calculated for four conditions (Cases 1–4) with two common sub-categories defined in Fig. 38.

Table 16 shows the experimental CG values and the corresponding CAD based values for the four test conditions shown in Fig. 38. It shows that minor shift in CG occurs due to the intake of water in the buoyancy chambers. It also shows that major shift in CG occurs due to moving mass mechanism.

6.1.2. Bifilar pendulum test

Bifilar pendulum test was conducted to determine mass moments of inertia of the glider about the vertical (I_{zz}) and binormal (I_{yy}) axes. The experimental values are compared with those obtained from the CAD model.

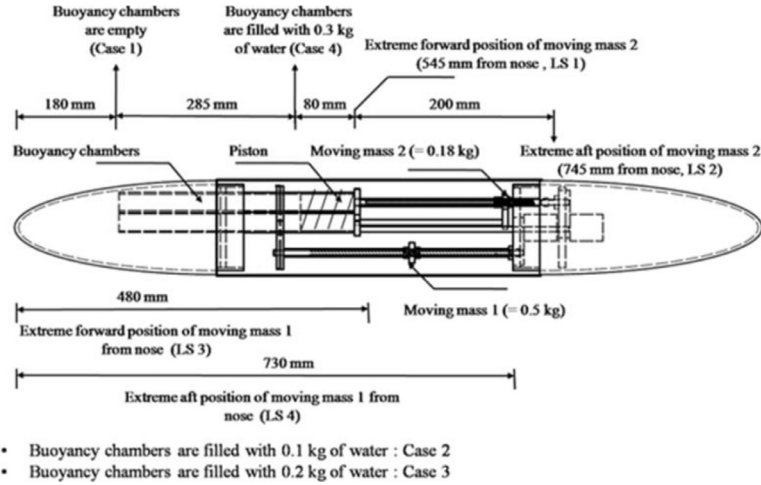


Fig. 38. Schematic drawing of test conditions.

Table 16
CG values for four test conditions.

M_1 (kg) (a)	M_2 (kg) (b)	Position of moving mass	M (kg) (a+b)	X_1 (cm)	X_2 (cm)	X (cm) Expt.	X (cm) CAD	Diff. (%)
Case 1								
7.51	8.28	LS 3	15.79	30	85	58.84	59.67	1.41
7.29	8.50	LS 4	15.79	30	85	59.61	60.45	1.41
Case 2								
7.53	8.36	LS 3	15.89	30	85	58.93	59.85	1.57
7.32	8.57	LS 4	15.89	30	85	59.66	60.56	1.52
Case 3								
7.56	8.43	LS 3	15.99	30	85	58.99	59.86	1.49
7.35	8.64	LS 4	15.99	30	85	59.72	60.57	1.43
Case 4								
7.58	8.51	LS 3	16.09	30	85	59.09	59.98	1.51
7.37	8.72	LS 4	16.09	30	85	59.81	60.68	1.47

To determine I_{zz} , the model is suspended by two strings of equal length so that CG lies halfway between the strings as shown in Fig. 39 and is set into swinging motion and period of one oscillation is computed using the accelerometer for three trials. Average time is used for final calculation. The details of the test are tabulated in Table 17. The moment of inertia, I_{zz} can be computed as:

$$I_{zz} = \frac{Wr^2t^2}{16\pi^2l} \quad (25)$$

The weight W includes the weight of rectangular clamps (4.31 N) and weight of round clamps (5.89 N) as shown in Fig. 39. Fig. 40 shows the test set up for determination of I_{zz} .

To ensure that stiffness of the string does not affect the result, steel strings are used. Fig. 41 shows the oscillations recorded from an accelerometer for 15 oscillations with a 100 Hz sampling rate.

Similar to the determination of I_{zz} , I_{yy} is determined by hanging glider with two strings parallel to the y-axis as shown in Fig. 43. The test set up is shown in Fig. 44. The details of test are tabulated in Table 18. Fig. 42 shows the reading of accelerometer to determine the time required for 15 cycles. δ_y is the angle subtended by glider x-axis.

In order to determine the mass moment of inertia around the x-axis (I_{xx}), glider has to be hanged with wings. Consider-

ing the fact that wings are fragile and cannot take up the load of the glider body, only CAD value of I_{xx} was considered and it had a value of 0.0869 kg m².

6.1.3. Rolling pendulum test

The vertical distance between CG and CB, l_d , is also of interest. It is important for gliders to have CB above CG to stabilize the vehicle in roll and pitch and make the vehicle more robust to disturbance. A test has been suggested in literature [16] to determine this using the following equation:

$$\omega_n^2 ml_d^2 - Wl_d + \frac{1}{2} \omega_n^2 m \left(\frac{d_b}{2} \right)^2 = 0 \quad (26)$$

where ω_n ($= 2\pi/t_n$) is the angular frequency, t_n is the time taken for two oscillations, d_b is the outer diameter of the glider hull (see Table 10), m is the mass of glider without ballast (see previous section) and $W=mg$. In this test, the vehicle without appendages (wings and rudder) was rolled 90° and allowed to damp to a small angle of 10°–15° and period was measured for two oscillations. A schematic diagram of the conducted experiment is shown in Fig. 45. The experiment was performed three times and average value of the time period was taken. Eq. (25) was solved for realistic roots within the design constraints. It was assumed that

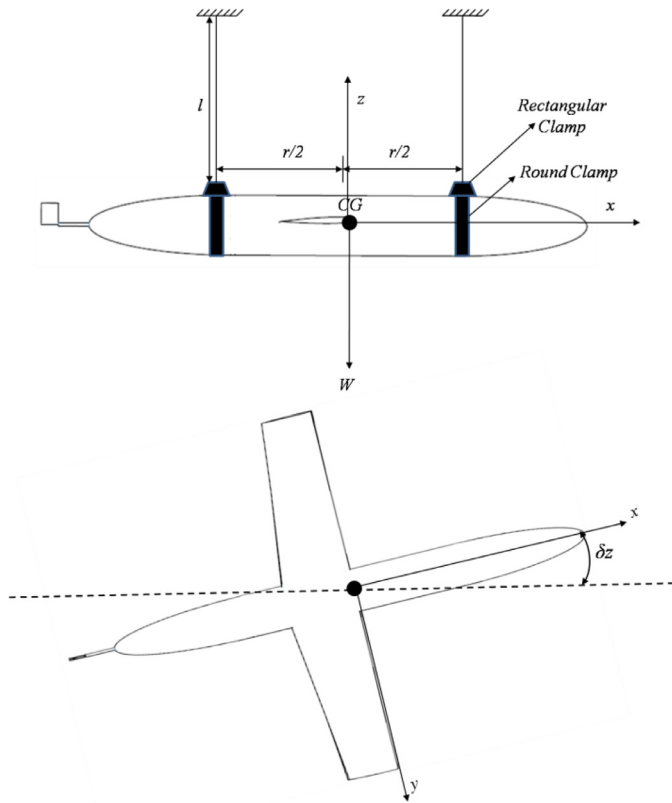


Fig. 39. Bifilar pendulum test setup to determine I_{zz} of the glider hull.

Table 17
Details for I_{zz} determination.

Trial	Time for 15 oscillations (s)	Time for 1 oscillation (s)	
1	28.97	1.93	$W = 160.622 \text{ N}$
2	28.20	1.88	$r = 0.38 \text{ m}$
3	28.77	1.91	$l = 0.46 \text{ m}$
I_{zz} (experimental)	1.17 kg m^2		
I_{zz} (CAD)	1.12 kg m^2		



Fig. 40. Test set up for determination of I_{zz} .

glider rotates about the centre line. The details of the test are tabulated in Table 19.

It was found that CG lies 4.57 mm below CB along the vertical axis. The value is validated against an equivalent CAD

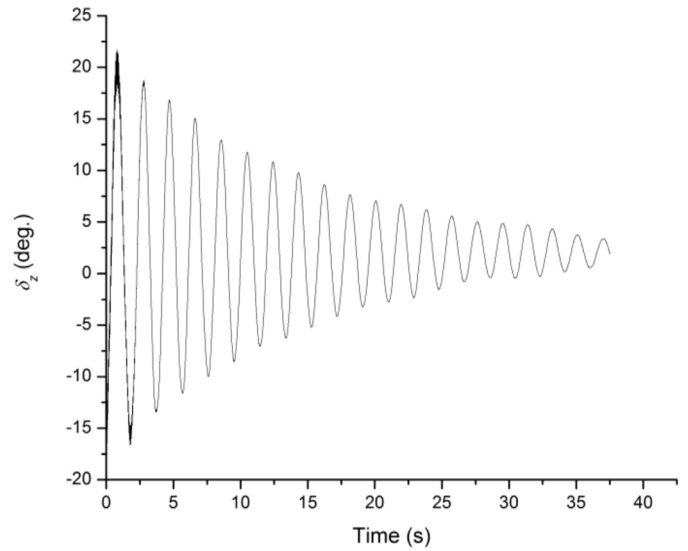


Fig. 41. Accelerometer reading for determination of I_{zz} .

Table 18
Details for I_{yy} determination.

Trial	Time for 15 oscillations (s)	Time for 1 oscillation (s)	
1	29.88	1.99	$W = 160.622 \text{ N}$
2	29.68	1.97	$r = 0.38 \text{ m}$
3	29.74	1.983	$l = 0.52 \text{ m}$
I_{yy} (experimental)	1.108 kg m^2		
I_{yy} (CAD)	1.08 kg m^2		

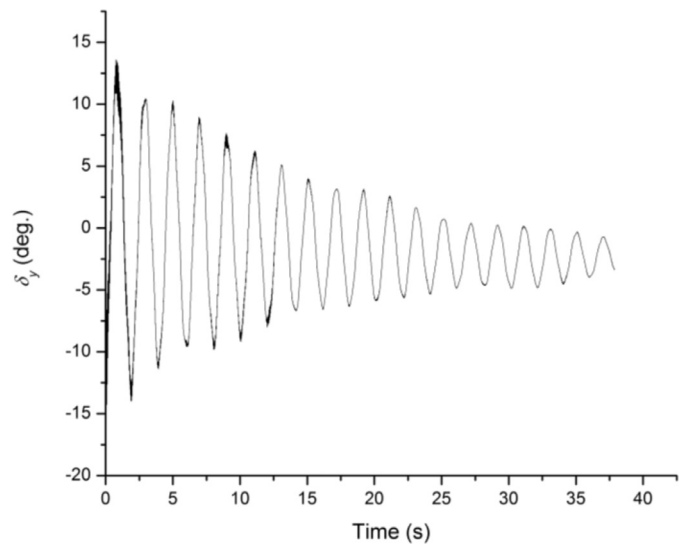


Fig. 42. Accelerometer reading for determination of I_{yy} .

model and positions of CG and CB within glider hull is represented in Fig. 46.

6.2. Calibration of pressure sensor

Pressure sensor was calibrated for both air and water. Fig. 47 shows the schematic set up of the sensor calibration

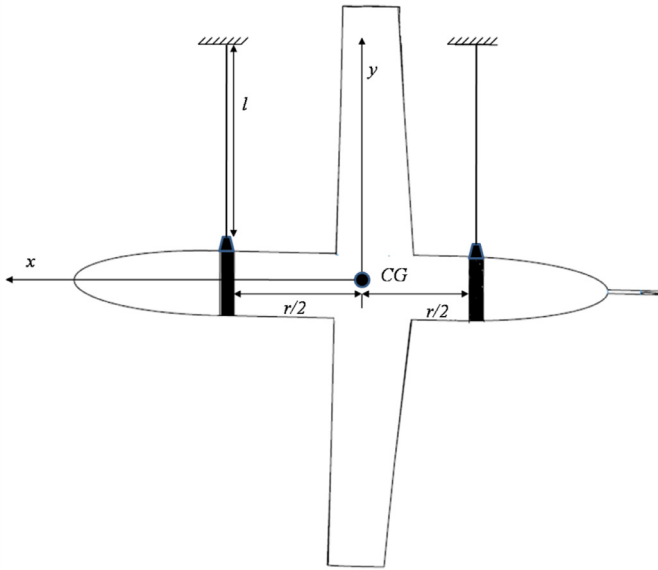


Fig. 43. Bifilar pendulum test setup to determine I_{yy} of the glider hull.

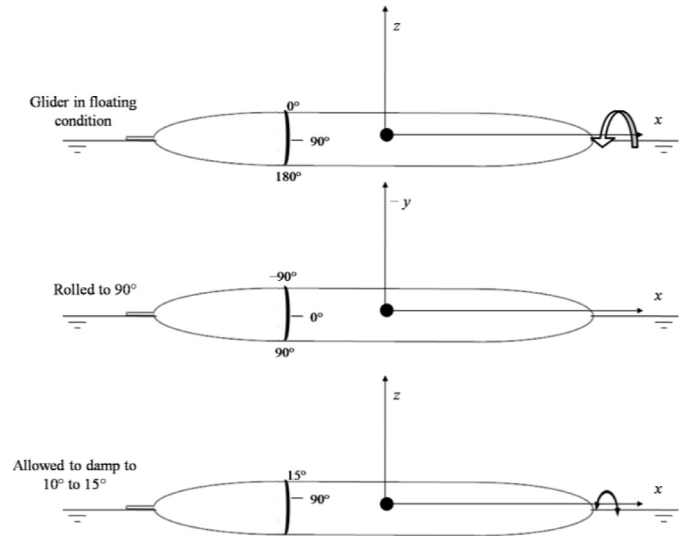


Fig. 45. Schematic of rolling pendulum test.



Fig. 44. Test set up for determination of I_{yy} .

Table 19

Details of rolling pendulum test.

Trial	t_n (s)	$W = 153.9$ N
1	1.45	$m = 15.39$ kg
2	1.5	$d_b = 0.14$ m
3	1.42	$\omega_n = (2\pi/1.46) = 4.30$ rad/s
Average time: 1.46		Solving Eq. (25), we get $l_d = 4.57$ mm (Expt.)
		$l_d = 4.74$ mm (CAD)

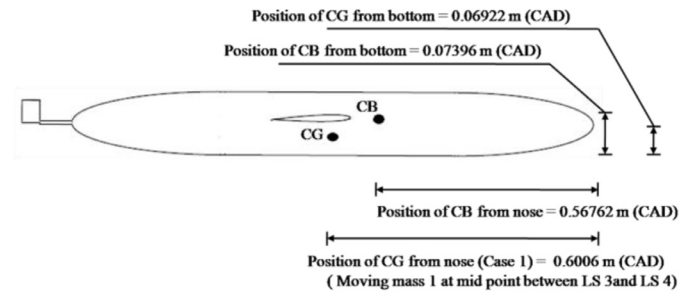


Fig. 46. Positions of CB and CG determined from CAD.

in air and the calibration curve (relationship between output voltage and applied pressure in air) is shown in Fig. 50. The curve is linear.

From Fig. 48, it can be seen that pressure sensor has a trend wherein 9 V is equivalent to 100 bar. This trend should be taken in account while making depth measurements using glider.

Fig. 49 shows the schematic setup for calibration of pressure sensor in water where the sensor is being fixed at the bottom part of a PVC pipe marked with a measuring (graduated) scale over its length to determine the depth of

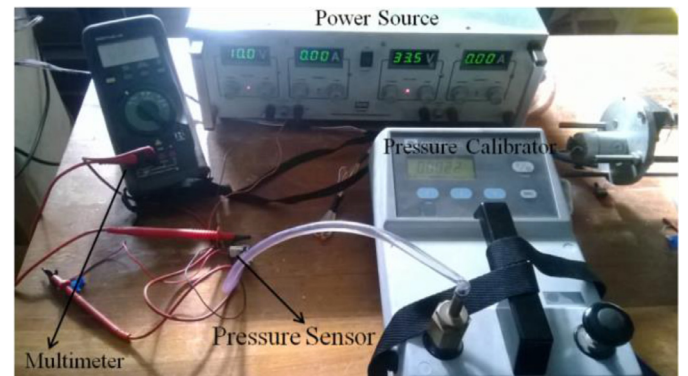


Fig. 47. Setup for pressure sensor calibration using air calibrator.

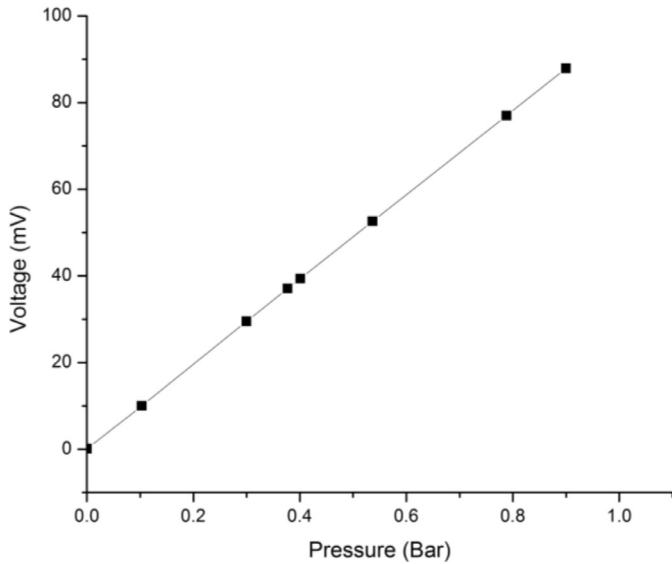


Fig. 48. Voltage against pressure for pressure sensor calibration in air.

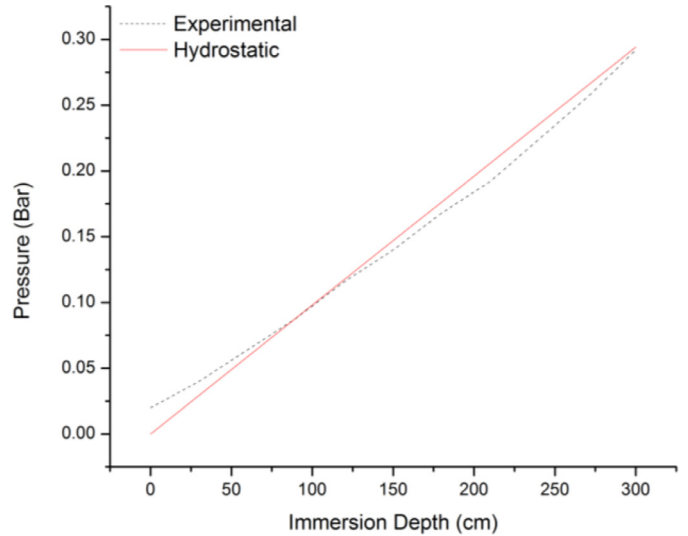


Fig. 50. Pressure values recorded by sensor against the hydrostatic pressure at the specified immersion depth.

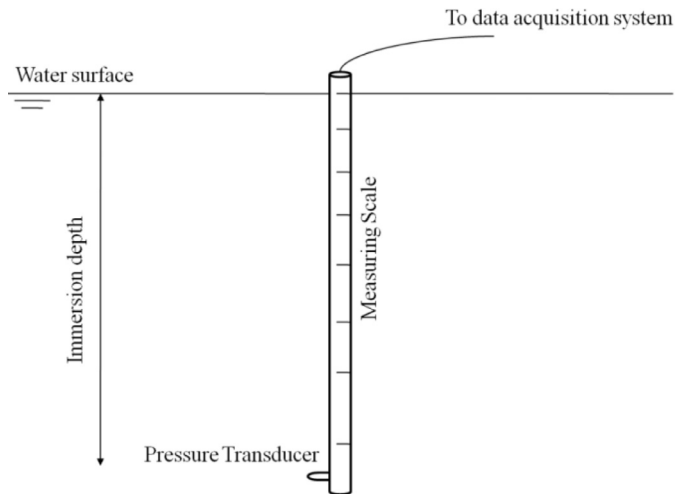


Fig. 49. Schematic setup for calibration of pressure sensor in water.



Fig. 51. Setup for calibration of inclinometer.

immersion. This calibration was performed in a 4 m wave flume at IIT Madras and results are shown in Fig. 50.

6.3. Calibration of inclinometer

Fig. 51 shows the calibration set up for the dual axis inclinometer which is mounted over a compass and the output voltage is noted for angles from -90° to $+90^\circ$ in steps of 5° . Fig. 52 shows the calibration for both X and Y axes (of the dual axis inclinometer) and the corresponding calibration constants.

6.4. Effect of moving mass and water intake on pitching angle

The effect of the moving mass mechanism and intake of water in buoyancy chamber on pitching have been shown in Fig. 53. It is seen that major change in pitching angle occurs

due to the intake of water in buoyancy chambers while minor change occurs due to the moving mass arrangement. The maximum angle subtended due to traverse of moving mass 1 from LS 3 to LS 4 is -9.42° while the maximum angle subtended due to the maximum intake of water in buoyancy chamber i.e. $\Delta B=0.3$ kg, for a fixed position of moving mass 1 at LS 3 is 26.75° .

6.5. Trajectory test

Pitch, roll and depth characteristics were measured during deployment trials of the glider in a flume of 4 m width and 2.5 m water depth and in a swimming pool of depth 5 m at IIT Madras. Pressure sensor and inclinometer were used for collecting the data.

The process of diving and surfacing in one cycle is as follows: (1) the moving mass 1 is brought forward to nose down the glider i.e. positioned at LS 3 and the piston begins to pump water into the buoyancy chamber, (2) the glider descends and reaches the required depth, (3) water is pumped out of the buoyancy chamber and the moving mass 1 is brought back to nose up the glider i.e. positioned at LS 4 and (4) the glider ascends and comes to the surface.

To simulate the equations of motion specified in second section, following parameters are used:

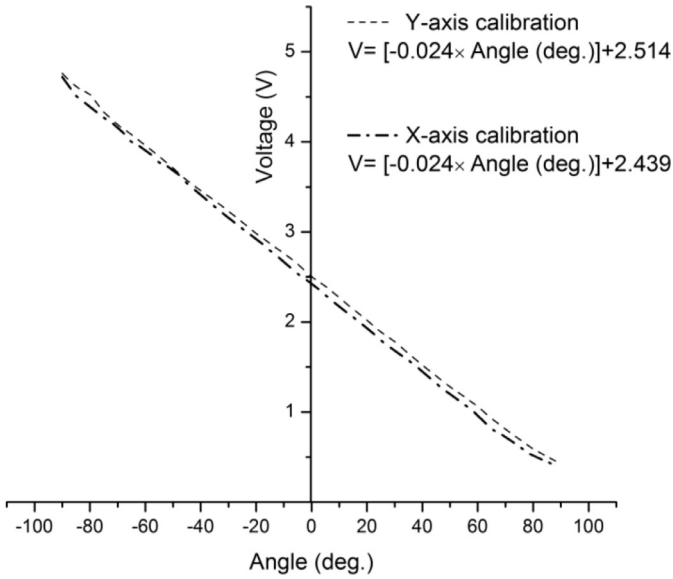


Fig. 52. X and Y-axis calibration of inclinometer.

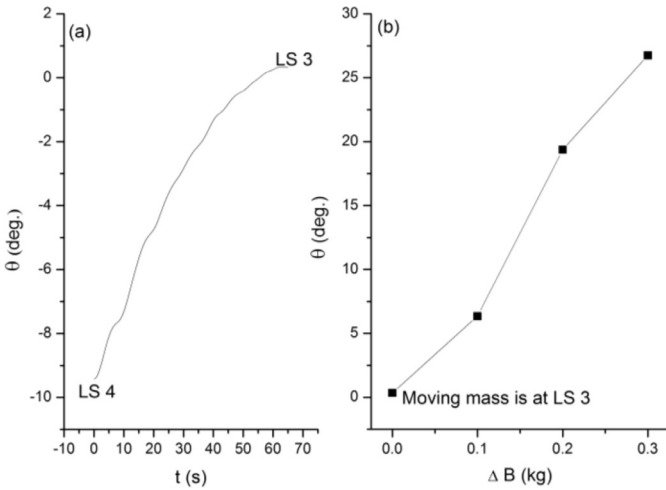


Fig. 53. Effect on pitching angle due to (a) moving mass traverse from LS 4 to LS 3 and (b) ΔB for a fixed position of moving mass at LS 3.

$u_b = \pm 15 \text{ g/s}$ (300 g of water can be sucked/ejected in 20 s)
 $u_{1x} = \pm 0.00006 \text{ kg m/s}^2$ $u_{2x} = \pm 0.0005 \text{ kg m/s}^2$, $u_{1z} = 0$ and $u_{2z} = 0$ (see Fig. 55)
 $K_{D0} = 2.8304 \text{ kg/m}$, $K_D = 0.02476 \text{ kg/m}$, $K_{L0} = 0.03538 \text{ kg/m}$,
 $K_L = 3.538 \text{ kg/m}$, $K_{M0} = 0.014152 \text{ kg/m}$ and $K_M = 0.14152 \text{ kg/m}$ (see CFD approach to steady state gliding)

$\Delta B = 0.3 \text{ kg}$
 $r_{1x} = 0.088 \text{ m}$ (Downward gliding), -0.162 m (Upward gliding)
 $r_{2x} = -0.177 \text{ m}$ (Downward gliding), 0.023 m (Upward gliding)
 (see Fig. 54)
 $r_{2z} = -0.03 \text{ m}$ (see Fig. 55)
 $r_{1z} = 0.03 \text{ m}$
 $r_{bx} = 0.285 \text{ m}$
 $r_{bz} = 0.07 \text{ m}$

$m_1 = 0.5 \text{ kg}$, $m_2 = 0.18 \text{ kg}$ (see Table 12)

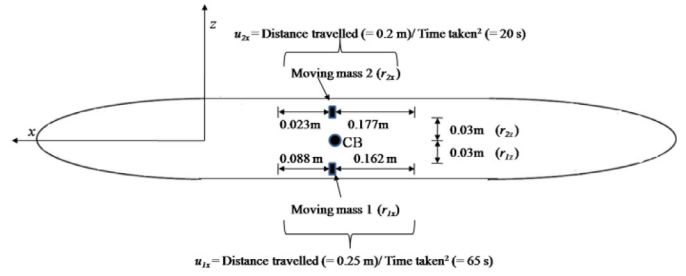


Fig. 54. Schematic showing parameters associated with simulation.

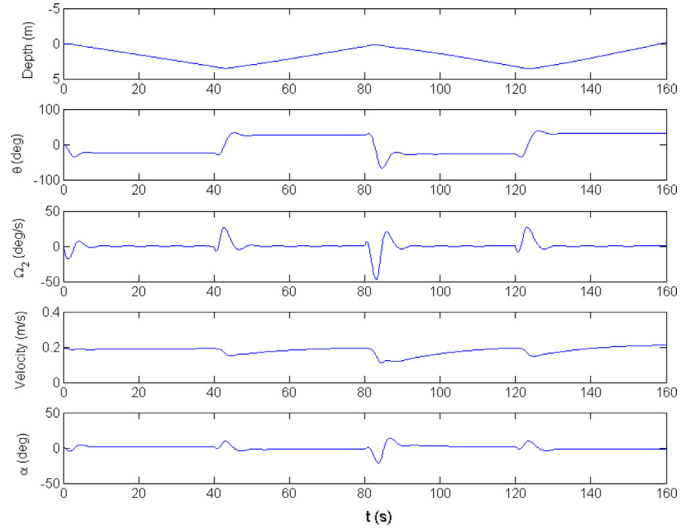


Fig. 55. Simulated parameters.

$m_{fx} = 0 \text{ kg}$ and $m_{fz} = 0 \text{ kg}$ (added mass terms are assumed to be zero)

$I_{yy} = 1.108 \text{ kg m}^2$ (see bifilar pendulum test)

$U = 0.198 \text{ m/s}$ (initial condition)

$\theta = \pm 26^\circ$ (initial condition: maximum angle in experiment)

The various parameters associated with simulation are shown in Fig. 54. The simulation results for several cycles are shown in Fig. 55.

6.5.1. Wave flume trial

Fig. 56 shows the pitch, roll and depth characteristics of glider during gliding test for one cycle conducted in the wave flume. From the data, one can see that high roll is observed while glider changes its orientation. This may be due to the fact that glider dynamics in transient state possesses overshoot oscillatory nature. It can be seen that due to the shallowness of the test tank, glider touches the bottom during shifting control from descend to ascend cycle.

6.5.2. Swimming pool trial

The glider was tested in the IIT Madras swimming pool having 5 m depth. Fig. 57 presents the measured pitch, roll and depth characteristics of the glider. It can be seen that pitch reaches a steady state value during its descent and ascent. High roll can be observed due to the effect of the wire on the glider motion. One can observe a sawtooth operating

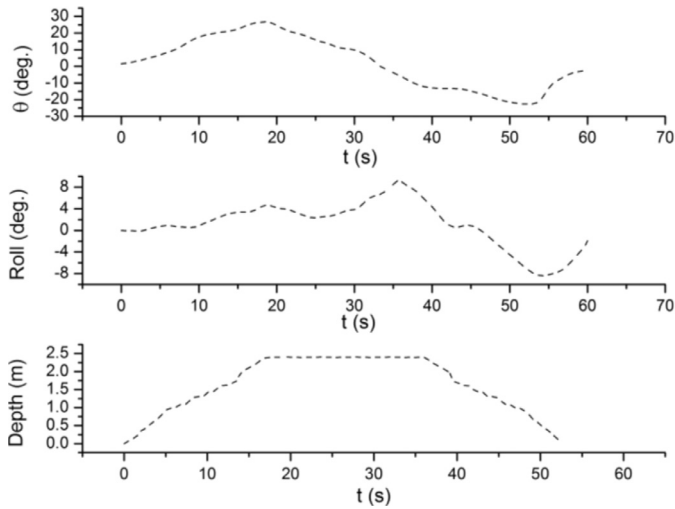


Fig. 56. Experimental data from gliding test in wave flume.

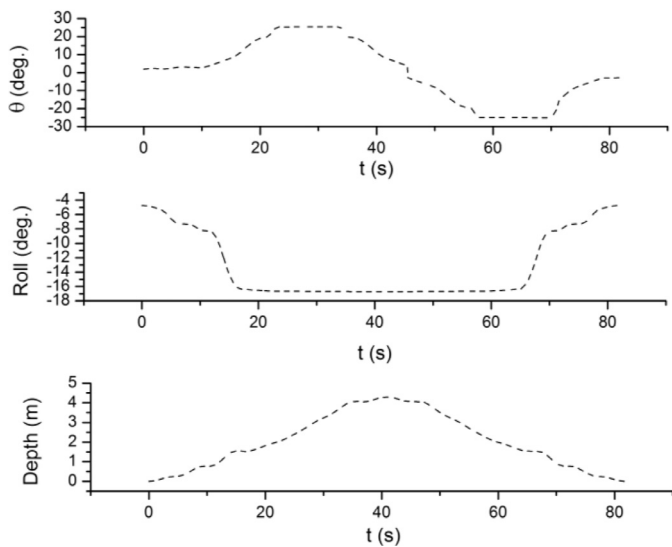


Fig. 57. Experimental data from gliding test in swimming pool.

profile from the depth readings obtained from experiments. Fig. 58 shows the comparison of experimental pitch and depth data against the simulation data obtained from the equations of motion. It shows that equations of motion predict the trend of pitch and depth well against the experimental data. The observed deviations are mainly due to the constraint of the wire. However, it is heartening to note that the depth compares very well despite this constraint. Fig. 59 shows the images showing the sequence of glider motion during swimming pool trials.

In this section, experimental determination of the non-hydrodynamic parameters of the glider is discussed and trials with the glider to obtain its trajectory are described. The parameters are verified against CAD model and the trajectory is compared with the results obtained from numerical simulation. The CAD model predicts the parameters well. The time variation of depth of the trajectory compares well with numerical simulation. However, the measured pitch angle has relatively poor match with simulation due to the fact that the

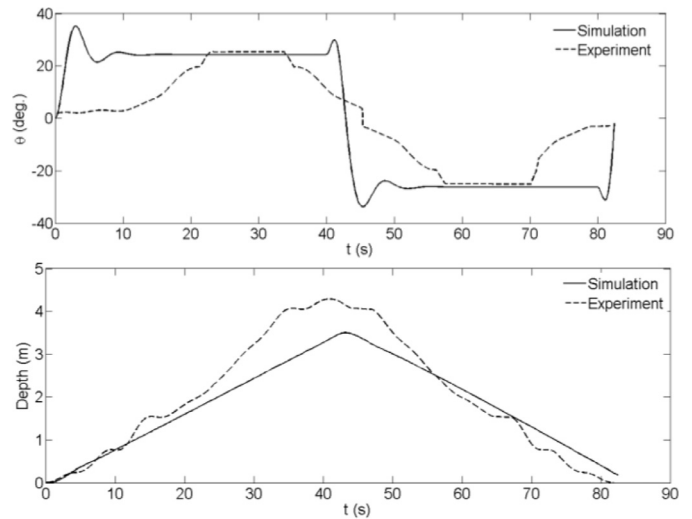


Fig. 58. Experimental and simulation results of gliding test in swimming pool.

glider is not ‘autonomous’ as assumed in the simulation, but has wires (cable) coming out from its tail for control of buoyancy engine and moving masses which provides restraint to the glider and affects its pitch and roll angles.

7. Conclusions and future work

The major conclusions of this study are as follows:

- CFD results of present work shows a far superior match with experimental results compared to CFD results of Ichihashi et al. [12].
- Symmetric wing profile gives an L/D ratio of 8 compared to unsymmetrical wing profile having an L/D ratio of 6. Hence, symmetric wing profile is more suited for better motion performance of underwater gliders.
- Larger change in buoyancy is desirable for efficient operation and longer range.
- CG test shows that major shift in CG occurs due to moving mass while minor shift occurs due to intake of water. A difference of less than 2% is observed between experimental and CAD values for four set of conditions.
- Bifilar test shows a difference of less than 5% between experimental and CAD values for mass moment of inertia along x and y axis. This shows that CAD models can be used in confidence for static and oscillation tests.
- Despite the constraint imposed by wire, depth data obtained from experiment compares very well with the depth results obtained from equations of motion. This shows that equations of motion can be used in confidence for predicting motion performance of the underwater gliders.

In order to remove the effect of the constraint imparted by wire, in future the glider should be made autonomous. In order to make the glider autonomous, a preprocessor should be installed within the hull of the glider and an

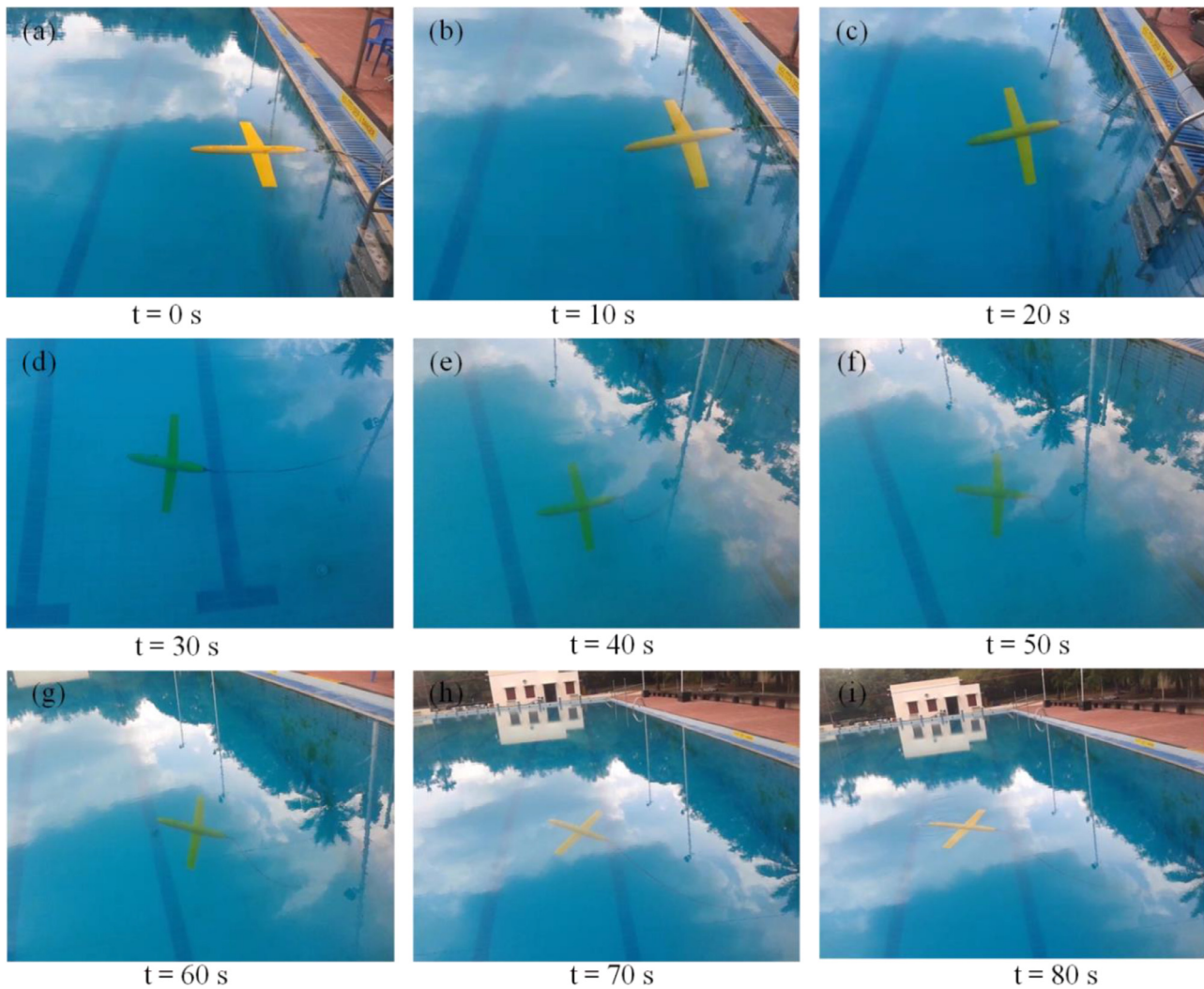


Fig. 59. Images of glider test in swimming pool.

appropriate control algorithm should be embedded within the preprocessor. The present design does not allow much space for installation of preprocessor within the hull. The length of the mid-section should be increased to accommodate preprocessor. Underwater communication is a major challenge in operation of gliders. There is a need to develop a multi-level wireless system in order to communicate with glider in operation. Gliders have limited communication during operation which leads to the need of a novel control system which can guide glider underwater effectively, with minimum control inputs. Effort should be made to design a bladder based buoyancy engine to test the performance of glider in deeper depths. Low drag shapes should be adopted for improved endurance and higher efficiency of gliders.

Acknowledgement

Authors would like to acknowledge the departmental grant received from Indian Institute of Technology, Chennai towards design and development of this model.

References

- [1] www.marine-knowledge.com/what-are-autonomous-underwater-vehicles, 2014.
- [2] Bagley, P.M., Player, M.A., and Jamieson, A.J. (2005). "A buoyancy control system", Patent no. W02005019021.
- [3] R. Davis, C. Eriksen, C. Jones, Technology and applications of autonomous underwater vehicles, 2002, pp. 1–11.
- [4] X.X. Du, B.W. Song, G. Pan, *Mechanika* 17 (4) (2011) 363–367.
- [5] C.C. Eriksen, T.J. Osse, R.D. Light, T. Wen, T.W. Lehman, P.L. Sabin, J.W. Ballard, A.M. Chiodi, *IEEE J. Ocean. Eng.* 26 (4) (2001) 424–436.
- [6] S.S. Fan, C.J. Yang, S. Peng, K. Li, Y. Xie, S. Zhang, *J. Zhejiang Univ.* 14 (8) (2013) 583–599.
- [7] J. Geisbert, Hydrodynamic modeling for autonomous underwater vehicles using computational and semi-empirical methods (Master's dissertation), Virginia Tech, 2007.
- [8] J. Graver, Underwater gliders: dynamics, control and design (PhD dissertation), Princeton University, 2005.
- [9] J. Graver, R. Bachmayer, N.E. Leonard, D.M. Fratantoni, in: Proceedings of the 13th International Symposium on unmanned untethered submersible technology (UUST), 2003.
- [10] J. Graver, J. Liu, C. Woolsey, N.E. Leonard, in: Proceedings of the conference on information sciences and systems (CISS), 1, 1998, pp. 1–6.

- [11] F.J. Harold, Variable buoyancy system metric (Master's dissertation), MIT, 2009.
- [12] N. Ichihashi, T. Ikebuchi, M. Arima, in: Proceedings of the eighteenth ISOPE conference, ISOPE 2008, Canada, 2008, pp. 156–161. ISBN: 1-880653-68-0
- [13] ITTC, Recommended procedures and guidelines: practical guidelines for ship CFD applications, 7.5, ITTC, 2011, pp. 1–18.
- [14] W. Jianguo, Z. Minge, S. Xiujun, Autonomous underwater vehicles, 2011 ISBN: 978-953-307-432-0.
- [15] N. Leonard, J. Graver, IEEE J. Ocean. Eng. 26 (4) (2001) 633–645.
- [16] A. Linklater, Design and simulation of a towed underwater vehicle (Ph.D. dissertation), Virginia Tech, 2005.
- [17] L. Lionel, Mobile robotics – towards new applications, 2006, pp. 335–360.
- [18] N. Mahmoudian, Efficient motion planning and control for underwater gliders (PhD dissertation), Virginia Tech, 2009.
- [19] A. Ray, S.N. Singh, V. Seshadri, in: Proceedings of conference on warship 2011 – naval submarines and UUVs, 2011 ISBN: 978-1-905040-86-5.
- [20] D.L. Rudnick, R.E. Davis, C.C. Eriksen, D.M. Fratantoni, M.J. Perry, Mar. Technol. Soc. J 38 (2) (2004) 73–84.
- [21] D.C. Seo, G. Jo, H.S. Choi, in: Proceedings of 18th MTS/IEEE Kobe-TECHNO-OCEAN'08, 2008, pp. 0–4.
- [22] J. Sherman, R. Davis, W.B. Owens, J. Valdes, IEEE J. Ocean. Eng. 26 (4) (2001) 437–446.
- [23] H. Stommel, Oceanography (1989) 22–25.
- [24] S. Tangirala, J. Dzielski, IEEE J. Ocean. Eng. 32 (4) (2007) 762–771.
- [25] M.C. Ting, M. Abdul Mujeebu, M.Z. Abdullah, M.R. Arshad, Indian J. Mar. Sci. 41 (2) (2012) 124–133.
- [26] Y. Wang, Y. Wang, Z. He, in: Proceedings of international conference on electronic and mechanical engineering and information technology, EMEIT 2011, 1, 2011, pp. 197–200.
- [27] D.C. Webb, P.J. Simonetti, C.P. Jones, IEEE J. Ocean. Eng 26 (4) (2001) 447–452.
- [28] M. Worall, J. Jamieson, N.R.D. Holford, M. Player, P.M. Bagley, in: Proceedings of OCEANS 2007 – Europe, 2007.
- [29] XCHAP Manual (2014). *SHIPFLOW User Guide*.
- [30] F. Zhang, T. John, T. Cody, T. Xiaobo, IEEE/ASME Trans. Mechatron. 19 (1) (2014) 394–399.
- [31] S. Zhang, J. Yu, A. Zhang, F. Zhang, Ocean Eng. 60 (2013) 1–13.
- [32] W.D. Zhao, J.A. Xu, M.J. Zhang, in: Proceedings of international conference on computer, mechatronics, control and electronic engineering, CMCE 2010, vol. 2, 2010, pp. 585–588.